CHIMERAS IN TWO-DIMENSIONAL DOMAINS: HETEROGENEITY AND THE CONTINUUM LIMIT

CARLO R. LAING

ABSTRACT. We consider three different two-dimensional networks of nonlocally coupled heterogeneous phase oscillators. These networks were previously studied with identical oscillators and a number of spatiotemporal patterns found, mostly as a result of direct numerical simulation. Here we take the continuum limit of an infinite number of oscillators and use the Ott/Antonsen ansatz to derive continuum level evolution equations for order parameter-like quantities. Most of the patterns previously found in these networks correspond to relative *fixed points* of these evolution equations, and we show here the results of extensive numerical investigations of these fixed points: their existence and stability, and the bifurcations involved in their loss of stability as parameters are varied. Our results answer a number of questions posed by previous authors who studied these networks, and provide a better understanding of these networks' dynamics.

1. INTRODUCTION

Chimera states, in which a nonlocally coupled network of similar oscillators splits into subgroups of synchronous and asynchronous oscillators, have been studied intensively over the previous decade [48, 18]. These states have been studied in networks of phase [2, 42, 50, 51, 4] and planar oscillators [22, 57, 19, 55, 7], using identical [36, 43, 64] or non-identical oscillators [21, 20, 24]. Networks studied include "point" networks [1, 52], and those which naturally exist in one-dimensional [3, 56, 40, 15], two-dimensional [37, 44, 66, 49, 47, 13] and even three-dimensional domains [30, 34]. Chimera states have also been observed in a number of experimental settings [59, 14, 39, 38].

In networks on two-dimensional domains a spiral wave chimera with an incoherent core is often observed [57, 19, 16, 66, 49, 44, 37]. Other patterns seen in two dimensions include stripe chimeras (equivalent to a chimera in one spatial dimension, but with no structure in the second dimension) [66, 44, 47] and spot chimeras, in which either coherent or incoherent oscillators form spatially localised spots [44, 49, 47]. Beyond pure simulation, previous analyses of these states include the following (in chronological order):

- Shima and Kuramoto [57] considered spiral wave chimeras on a two-dimensional lattice of phase oscillators with free boundary conditions and derived a self-consistency equation, similar to that derived by Kuramoto [17, 58] for an all-to-all coupled network. They numerically solved this equation and found that the results obtained were in good agreement with simulations of the original network.

Date: December 29, 2016.

2000 *Mathematics Subject Classification.* 34C15, 37G35, 34D06, 35B36.

Key words and phrases. chimera, coupled oscillator, Kuramoto, spiral, Ott/Antonsen, bifurcation.

- Laing [21] considered a finite two-dimensional lattice of non-identical phase oscillators with nonlocal coupling which was normalised to account for the domain boundaries. He used the Ott/Antonsen ansatz [45, 46] to derive a set of evolution equations for the expected value of the (complex) order parameter at each lattice point and followed the fixed points of these equations corresponding to a spiral chimera as the phase shift in the coupling function was varied. The stability of the spiral wave was determined by linearising the evolution equations around it, and the spiral wave was seen to become unstable as the phase shift parameter was varied.
- Martens et al. [37] considered identical oscillators on an unbounded planar domain and analysed a self-consistency equation, similar to that derived by Kuramoto [17, 58], describing a spiral wave in a network consisting of an infinite number of oscillators. These authors found approximate expressions for the rotation speed of the spiral and the size of its incoherent core as a function of the system's one parameter (the phase shift in the coupling function).
- Panaggio and Abrams [47] considered a two-dimensional domain with periodic boundary conditions in both directions (a "flat torus") and a D_4-symmetric coupling function and analysed a self-consistency equation like that derived by Kuramoto. They used numerical simulations to determine the stability of solutions and obtained stable spot and stripe chimeras, like those observed in [44]. Their main result was showing that such solutions are connected by unstable chimeras with less symmetry than the stable solutions just mentioned.
- In a later paper Panaggio and Abrams [49] considered identical oscillators on a sphere and analysed a self-consistency equation like that derived by Kuramoto. They considered the two limits of localised and near-global coupling, the taking of which simplified the self-consistency equations for both spot and spiral chimeras. They derived a number of approximate expressions for quantities such as fraction of drifting (i.e. asynchronous) oscillators. They also performed numerical continuation on the self-consistency equations and determined stability of the resulting solutions via direct numerical simulation of a large network of oscillators.
- Xie et al. [66] also considered identical oscillators on a "flat torus" with two specific D_4-symmetric coupling functions. They exploited the form of the coupling functions to describe analytically a variety of states such as splay, twisted chimera and spiral chimera, and to derive algebraic equations for the eigenvalues describing the stability of these states. For one coupling function they found time-dependent "crescent structures" in the cores of spiral waves but were unable to provide a full understanding of them.

Here we consider three systems similar to those studied in [66, 49, 44]. The main difference between the models studied here and those in [66, 49, 44] is that we consider heterogeneous networks, in which the intrinsic frequencies of oscillators are nonidentical (to be precise, they are chosen from Lorentzian distributions). There are several reasons for doing this:

(a) The Ott/Antonsen ansatz [45, 46], which we use extensively, is only valid when phase oscillators are non-identical.
(b) Networks of identical sinusoidally coupled phase oscillators are known to have non-generic behaviour [62, 63], and previous experience [20, 21] with heterogeneous networks suggests that heterogeneity "unfolds" this non-generic behaviour, leaving only generic behaviour and generic bifurcations.

(c) Following on from the previous point, in order to use standard numerical bifurcation analysis algorithms [26, 10], the system under study should be generic, and not have any conserved quantities, for example, nor continuous spectra on the imaginary axis [64, 42].
(d) One could argue that heterogeneous systems are better models of reality than highly-symmetric homogeneous systems.

Our approach is also different from those taken in [66, 49, 44], where finite networks of oscillators were simulated. Here we take the continuum limit of an infinite number of oscillators and use the Ott/Antonsen ansatz to derive evolution equations for complex order parameter-like quantities. One advantage of this approach is that all solutions of interest (apart from the "crescent structures" in Sec. 3) are relative *fixed points* of these evolution equations (specifically, fixed points in a rotating coordinate system). We can thus discretise these evolution equations in standard ways, find fixed points of the resulting large set of integro-differential equations, and follow these fixed points as parameters are varied, determining fixed points' stability from the eigenvalues of the appropriate (large) matrices. Another advantage of this approach is that we avoid the issue of a chimera in a finite network of oscillators being numerically stable when the number of oscillators is large, but unstable when fewer oscillators are used, as is known to occur [65].

This approach allows us to, for example, precisely determine the regions of existence of spiral wave chimeras in models similar to those studied in [49, 44], and to show that the boundaries of these regions correspond to Hopf bifurcations of the spirals. (The boundaries were found approximately in [49, 44] by repeatedly simulating large networks of oscillators at many points in a parameter plane, and deciding at each point whether or not the simulation showed a stable spiral chimera.) We also study a model similar to that in [66] in which the authors found dynamic "crescent structures" for one form of coupling but not another. They noted that such structures seem associated with a core instability of a spiral, but could not find evidence for such an instability. By interpolating between the two coupling functions used in [66] we provide strong evidence that these crescent structures *do* arise from a Hopf bifurcation of rigidly rotating spiral waves. We also show that the coherent and incoherent spots found by [44] form a continuous family, and determine where in parameter space they (and stripe solutions) are stable, and the bifurcations they undergo as parameters are varied. (Panaggio and Abrams [47] also found that coherent and incoherent spots form a continuous family, although they considered a different coupling kernel from that of [44].)

The structure of the paper is as follows. We consider oscillators on a sphere, as did [49], in Sec. 2. Spot solutions are investigated in Sec. 2.2 and spirals in Sec. 2.3. In Sec. 3 we consider a model similar to that of [66], consisting of oscillators on a flat torus, with D_4-symmetric coupling. In Sec. 4 we consider a model similar to that of [44], also on a flat torus, but with a circularly-symmetric coupling kernel. Spiral waves are considered in Sec. 4.1 and spots and stripes in Sec. 4.2. We conclude in Sec. 5, and the Appendices contain extra relevant information.

2. Oscillators on a sphere

We consider a system of heterogeneous Kuramoto oscillators on the unit sphere $\mathbb{S}^2$, similar to that studied in [49], which can be written compactly as

$$\frac{\partial\psi(\mathbf{r})}{\partial t} = \omega(\mathbf{r}) - \int_{\mathbb{S}^2} G(\mathbf{r},\mathbf{r}')\sin\left(\psi(\mathbf{r}) - \psi(\mathbf{r}') + \alpha\right)d\mathbf{r}' \tag{1}$$

where $\psi(\mathbf{r}) \in [0, 2\pi)$ is the phase of an oscillator at position $\mathbf{r}$, α is a phase shift parameter, and $G(\mathbf{r}, \mathbf{r}')$ is the coupling kernel, governing the strength of coupling from oscillators at position $\mathbf{r}'$ to oscillators at position $\mathbf{r}$. In practice we study a spatial discretisation of (1), and the related equation (3) resulting from taking the continuum limit of this discretisation. At each point in space, $\omega(\mathbf{r})$ is chosen independently and randomly from the Lorentzian distribution with width Δ, centred at $\omega = 0$:

$$g(\omega) = \frac{\Delta/\pi}{\omega^2 + \Delta^2} \tag{2}$$

Then taking the continuum limit as the discretisation becomes finer and finer, one can use the Ott/Antonsen ansatz [46, 45] and the properties of the Lorentzian to describe the dynamics of (1) in terms of the following equation for a complex, spatially-dependent order parameter $z(\mathbf{r}, t)$:

$$\frac{\partial z(\mathbf{r}, t)}{\partial t} = -\Delta z(\mathbf{r}, t) + e^{-i\alpha} Z(\mathbf{r}, t)/2 - e^{i\alpha} z^2(\mathbf{r}, t)\overline{Z}(\mathbf{r}, t)/2 \tag{3}$$

where an overbar indicates complex conjugate and

$$Z(\mathbf{r}, t) = \int_{\mathbb{S}^2} G(\mathbf{r}, \mathbf{r}') z(\mathbf{r}', t) d\mathbf{r}' \tag{4}$$

Such derivations have been performed in a number of previous publications [21, 23, 41, 42, 64, 44] and we refer the interested reader to those. To give a physical meaning to $z(\mathbf{r}, t)$, we note that the distribution of oscillator phases, ψ, at position $\mathbf{r}$ and time t is [42, 21]

$$P(\psi) = \frac{1 - |z|^2}{2\pi \left[1 - 2|z| \cos\left(\psi - \arg z\right) + |z|^2\right]} \tag{5}$$

which is a unimodal distribution centred at $\psi = \arg z$. The sharpness of this distribution depends on $|z|$: $|z| = 0$ corresponds to a uniform distribution (i.e. incoherence), and as $|z| \to 1$, $P(\psi) \to \delta(\psi - \arg z)$, the Dirac delta function.

It is well-known that many solutions of interest of (3) are stationary in a rotating coordinate frame, and in this coordinate frame (3) is replaced by

$$\frac{\partial z(\mathbf{r}, t)}{\partial t} = -(\Delta - i\Omega) z(\mathbf{r}, t) + e^{-i\alpha} Z(\mathbf{r}, t)/2 - e^{i\alpha} z^2(\mathbf{r}, t)\overline{Z}(\mathbf{r}, t)/2 \tag{6}$$

where Ω is the frequency of rotation, which generally depends on the parameters of the system and the particular solution under consideration.

As in [49] we will use the Fisher-von Mises function:

$$G(\mathbf{r}, \mathbf{r}') = \frac{\kappa e^{\kappa(\mathbf{r}\cdot\mathbf{r}')}}{4\pi \sinh \kappa} = \frac{\kappa e^{\kappa \cos\gamma}}{4\pi \sinh \kappa} \equiv B(\gamma) \tag{7}$$

where γ is the central angle between $\mathbf{r}$ and $\mathbf{r}'$. Thus the strength of coupling between oscillators at $\mathbf{r}$ and $\mathbf{r}'$ depends only on the great circle distance between these points. The coupling becomes more localised as $\kappa \to \infty$, and $\lim_{\kappa \to 0} B(\gamma) = 1/(4\pi)$, giving global coupling. We will use a coordinate system in which $\theta \in [0, \pi]$ is the polar angle and $\phi \in [0, 2\pi)$ is the azimuthal angle. (Note that this is the opposite convention from [49].)

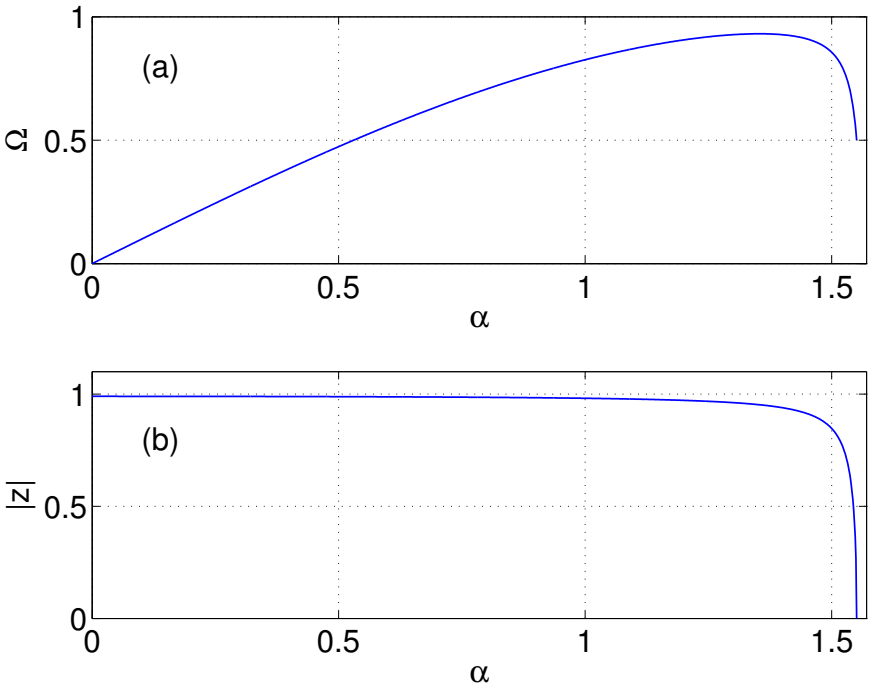

FIGURE 1. Spatially uniform states given by (9). (a): Ω as a function of α; (b): $|z|$ as a function of α. Parameters: $\Delta = 0.01$.

2.1. **Spatially uniform states.** We first consider spatially uniform states. Since $\int_{\mathbb{S}^2} G(\mathbf{r},\mathbf{r}')d\mathbf{r}' = 1$ these satisfy

$$0 = -(\Delta - i\Omega)z + e^{-i\alpha}z/2 - e^{i\alpha}z^2\overline{z}/2. \tag{8}$$

$z = 0$, corresponding to the incoherent state, is obviously always a solution of (8). Linearising (6) about this state, and only considering spatially uniform perturbations, we find that it is unstable for $2\Delta < \cos\alpha$ and stable otherwise. The other solution of (8) is given by

$$|z| = \sqrt{1 - \frac{2\Delta}{\cos\alpha}}; \qquad \Omega = \sin\alpha - \Delta\tan\alpha \tag{9}$$

plotted in Fig. 1. Linearising (6) about this state we find it to be stable with respect to spatially uniform perturbations for $2\Delta < \cos\alpha$, i.e. when it exists.

2.2. **Rotationally invariant states.** These solutions are independent of ϕ and thus the complex variable of interest is $z(\theta,t)$, where $0 \le \theta \le \pi$. (Recall that $\theta \in [0,\pi]$ is the polar angle and $\phi \in [0,2\pi)$ is the azimuthal angle; the opposite convention from [49].) Expanding in Legendre polynomials of $\cos\theta$ as

$$z(\theta,t) = \sum_{l=0}^{\infty} \sqrt{\frac{2l+1}{4\pi}} z_l(t) P_l(\cos\theta) \tag{10}$$

we have

$$Z(\theta,t)=\sum_{l=0}^{\infty}\sqrt{\frac{2l+1}{4\pi}}Z_l(t)P_l(\cos\theta) \tag{11}$$

where (see Appendix A)

$$Z_l(t)=b_l z_l(t)\sqrt{\frac{4\pi}{2l+1}} \tag{12}$$

and

$$b_l=\frac{\sqrt{2\kappa(2l+1)}}{4\sinh\kappa}I_{l+1/2}(\kappa) \tag{13}$$

where I_s is the modified Bessel function of the first kind of order s. Thus the equation of interest is

$$\frac{\partial z(\theta,t)}{\partial t}=-(\Delta-i\Omega)z(\theta,t)+e^{-i\alpha}Z(\theta,t)/2-e^{i\alpha}z^2(\theta,t)\overline{Z}(\theta,t)/2 \tag{14}$$

where $Z(\theta,t)$ is given by (11). For numerical computations, we discretised θ as $\theta_i=(i/200)\pi$ for $i=0,1,\dots 200$ and truncated (10) and (11) at $l=20$. At any instant in time t, given $z(\theta,t)$ the $z_l(t)$ are found by approximating an integral of the form (61), these are inserted into (12) to give the $Z_l(t)$, and these are used in (11) to approximate $Z(\theta,t)$.

A typical stable stationary solution of (14) is shown in Fig. 2, with $\Omega\approx 0.68$. This solution was found by numerically integrating (14) with an initial condition similar in form to that shown in Fig. 2. Note that if $z(\theta)$ is a stationary solution of (14), so is $z(\theta)e^{i\beta}$ for any constant β (which is just a reflection of the fact that (1) depends on only phase differences) so we choose one solution from this continuous family by imposing that

$$\arg(z(0))=0. \tag{15}$$

Appending (15) to (14) (with $\partial z/\partial t=0$) allows us to simultaneously solve these equations for $z(\theta)$ and Ω using Newton's method, for example.

From Fig. 2 (a) we see that for this solution, $|z|\approx 1$ (corresponding to near-coherence) over less than half of the domain, so this solution could be referred to as a "coherent spot" solution. This is confirmed by Fig. 2 (b) where we plot (on a log scale) the probability density given in (5) for the $z(\theta)$ shown in Fig. 2 (a). Since the oscillators are not identical, i.e. $\Delta>0$, we will never obtain complete locking, with $|z|=1$. However, as $\Delta\to 0$ we find that $|z|\to 1$ for $0\le\theta\lesssim 0.8$ (the coherent region) and we obtain a plot of $|z|$ as a function of θ similar to those shown in [42, 64, 21], for example.

2.2.1. *Numerical continuation.* The results of following the solution shown in Fig. 2, and the spatially uniform state, as α is varied are shown in Fig. 3. We see that the spot becomes unstable through a saddle-node bifurcation as α is decreased and through a Hopf bifurcation as α is increased. The branch of spots terminates on the branch of spatially uniform states, which changes stability as α is varied. (Stability is as a solution of (14), where θ-dependent perturbations are considered.)

Following the bifurcations from Fig. 3 as both α and κ are varied we obtain Fig. 4. The curves of codimension-one bifurcations divide the parameter plane into five regions (a,b,c,d and e) and these curves meet at three codimension-two points (A,B and C). Point A is a Takens-Bogdanov (double-zero) bifurcation: to the left of it, the saddle-node bifurcation creates two unstable solutions as κ is increased, whereas to the right of A, one stable and one unstable spot solution are created as κ is increased. At

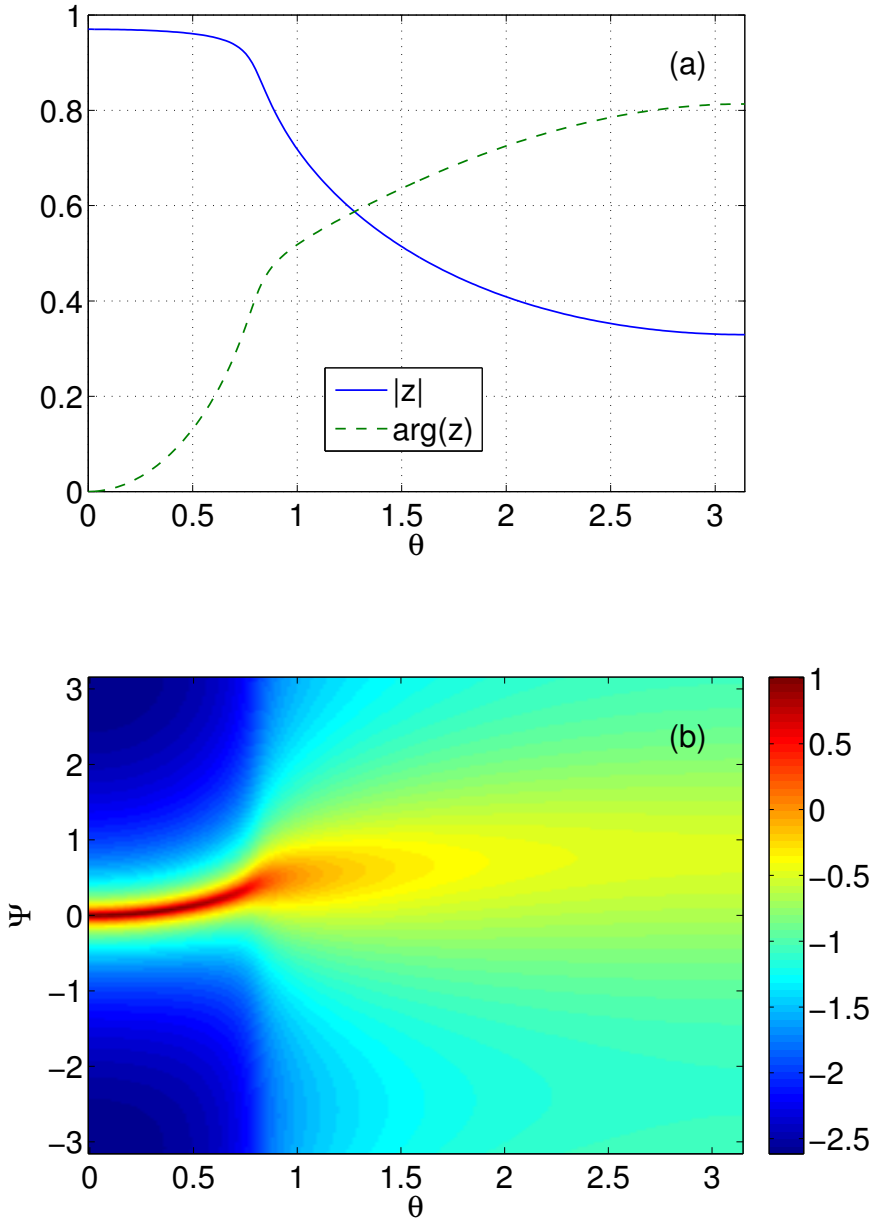

FIGURE 2. Typical stable coherent spot solution of (14). (a): $|z|$ (solid) and $\arg z$ (dashed) as functions of θ. (b): the log (base 10) of the probability density function (5) for the solution in panel (a). Parameters: $\kappa = 2, \Delta = 0.01, \alpha = 1.45$.

points B and C the criticality of the bifurcation from the uniform state changes: between B and C it is supercritical and a stable spot is created as κ is increased.

A stable single spot solution exists in regions b and c, created as κ increases through either a supercritical bifurcation from the spatially uniform state (between B and C) or in a saddle-node bifurcation

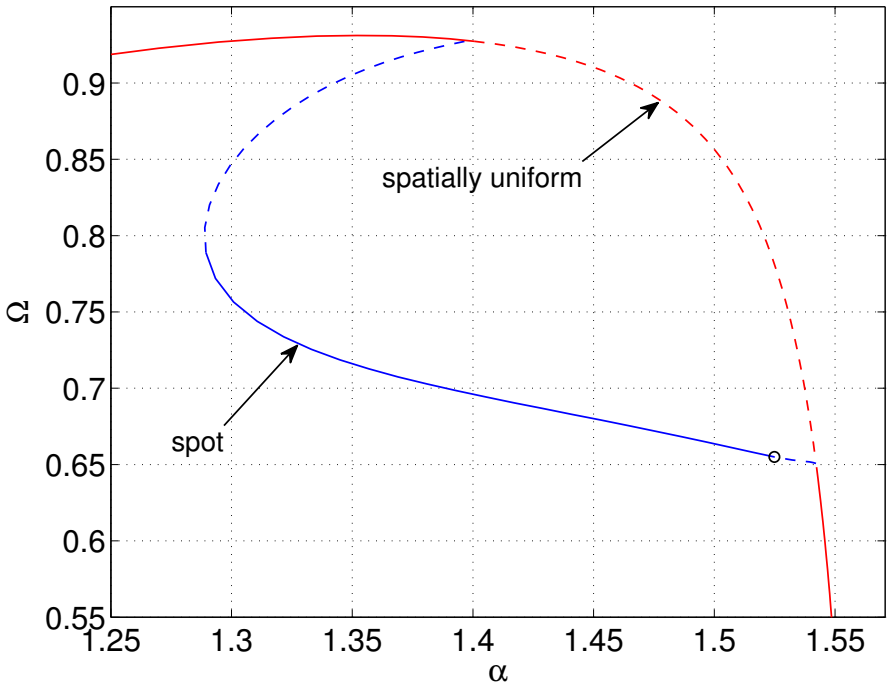

FIGURE 3. Continuation of the solution shown in Fig. 2, and the spatially uniform state, as α is varied. Solid: stable, dashed: unstable. The Hopf bifurcation is shown with a circle. Parameters: $\Delta = 0.01, \kappa = 2$.

(between A and B). A spatially uniform state may be stable in regions a,b and d. (We cannot be sure, as we have not considered all types of perturbations.) The Hopf bifurcation appears to be subcritical, and an example of the dynamics just past it are shown in Fig. 5. Numerically, this solution appears to be spatiotemporally chaotic.

Panaggio and Abrams [49] derive the expression $\pi/2 - \alpha \approx 0.0915\kappa$ for a saddle-node bifurcation of a single spot solution in the limit $\kappa \ll 1$ (and $\Delta = 0$). By following the curve of saddle-node bifurcations shown in Fig. 4 for smaller and smaller values of Δ we found that the point B did approach $(\alpha, \kappa) = (\pi/2, 0)$, but that the curve of saddle-node bifurcations, near B, was better fit by the expression $\pi/2 - \alpha \approx 0.14\kappa$. We currently have no explanation for this discrepancy. (Using a finer discretisation of (14), or including more terms before truncating (10) and (11) does not change the observed results.) These authors did not mention Hopf bifurcations of spots, which do occur when the full dynamics on the sphere are simulated using the scheme presented below. There are several possible reasons for this: (i) the Hopf bifurcations do not occur for identical oscillators, i.e. when $\Delta = 0$; (ii) the Hopf bifurcations do occur for identical oscillators, but these authors did not specifically look for this type of instability of a spot.

2.2.2. *Other solutions.* Figure 4 is not a complete description of solutions of (14), as this equation can also support, for example, a "double spot" solution such as that in Fig. 6. This solution is symmetric

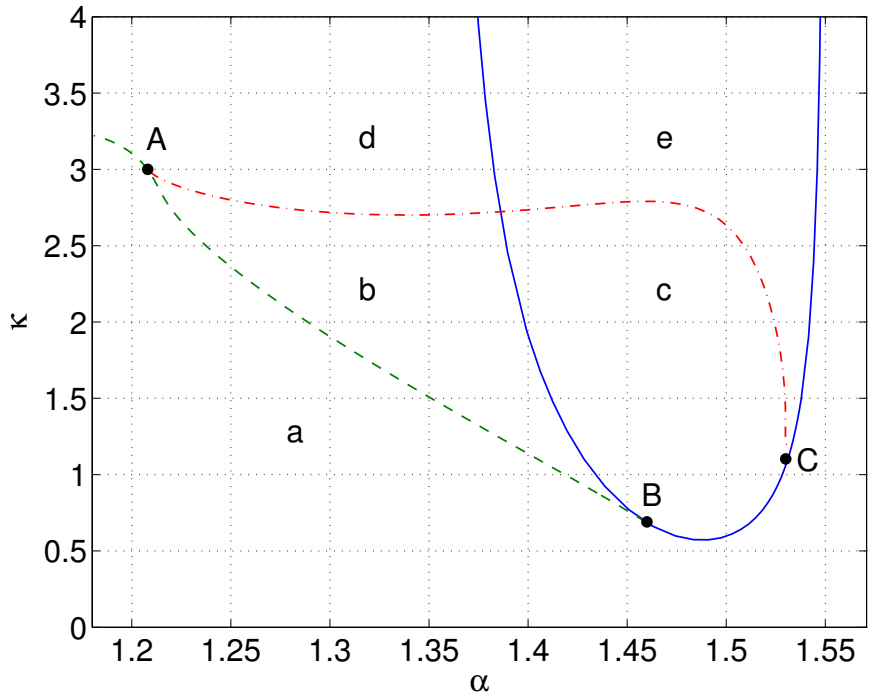

FIGURE 4. Bifurcations of single spot solutions of (14). Solid: instability of spatially uniform state to single spot solution. Dashed: saddle-node bifurcation of single spot solution. Dash-dotted: Hopf bifurcation of single spot solution. For $\alpha > \cos^{-1}(2\Delta) \approx 1.5508$ $z = 0$ is stable, and unstable otherwise. Fig. 3 is a horizontal "slice" through this figure at $\kappa = 2$. See text for explanation of labels. Parameters: $\Delta = 0.01$.

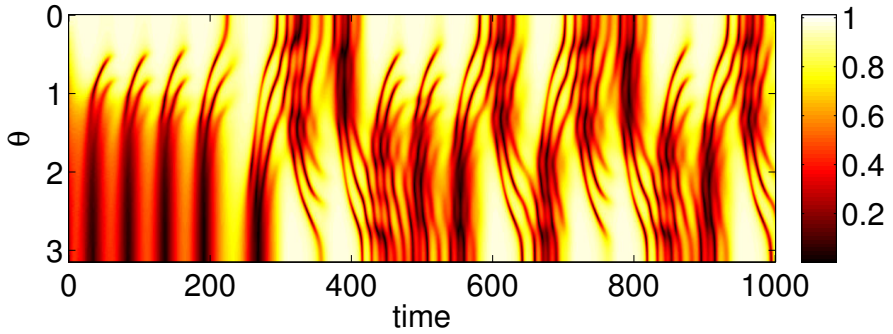

FIGURE 5. Dynamics of (14) just above the Hopf curve in Fig. 4. $|z|$ is shown in colour. Parameters: $\kappa = 2.8, \alpha = 1.45, \Delta = 0.01$.

about $\theta = \pi/2$ and has two regions of near-coherence, one at each pole. Its similarity with that shown in Fig. 2 of [21] is striking. Such solutions could also be followed as parameters are varied, but we do not pursue that here.

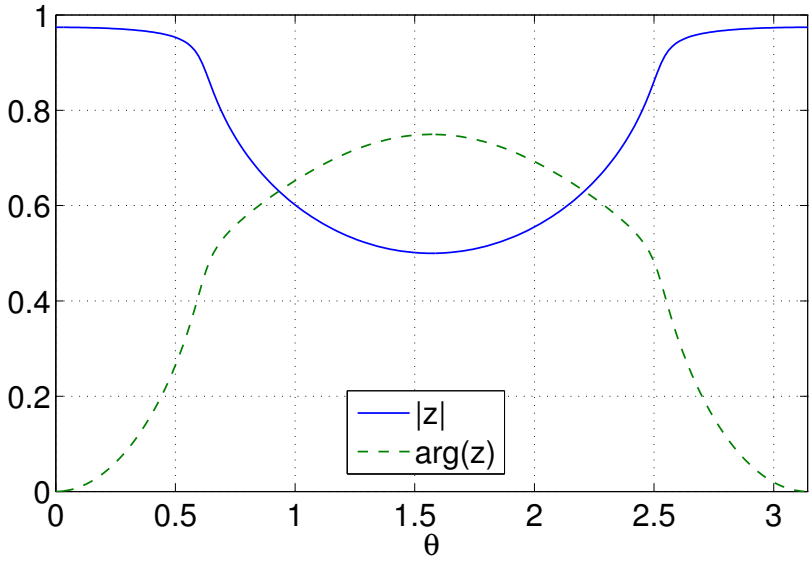

FIGURE 6. A stable double spot solution of (14) with $\Omega \approx 0.71551$. Compare with Fig. 2 (a). Parameters: $\kappa = 4, \alpha = 1.45, \Delta = 0.01$.

By only considering (14) we cannot determine the stability of solutions of this equation with respect to perturbations which depend on ϕ. In particular, it is not clear that our results will carry over to the full system (6). In principle we could linearise (6) about a steady state of (14) to determine its stability, but the resulting calculations seem significantly more difficult than those in [64, 42, 41] (where only one spatial dimension is considered) and [61] (in which only the stability of a spatially uniform state is considered) and we do not pursue this further. However, numerical solutions on the full sphere (using the scheme presented below) indicate that the double spot solution in Fig. 6 is actually unstable in this context, but for the parameters used in Fig. 5 there is a chaotic solution which is circularly symmetric (like that in Fig. 5) which is *stable* with respect to perturbations which break this symmetry. This is an example of a solution which is chaotic when restricted to the invariant subspace of circularly-symmetric solutions, but is stable with respect to perturbations out of that subspace; see [5] for an example of this behaviour in the complex Ginzburg-Landau equation.

2.3. **Spiral chimeras.** We now consider (6), written in spherical polar coordinates as

$$\frac{\partial z(\theta,\phi,t)}{\partial t} = -(\Delta - i\Omega)z(\theta,\phi,t) + e^{-i\alpha}Z(\theta,\phi,t)/2 - e^{i\alpha}z^2(\theta,\phi,t)\overline{Z}(\theta,\phi,t)/2. \tag{16}$$

Expanding $z(\theta,\phi,t)$ in spherical harmonics as

$$z(\theta,\phi,t) = \sum_{k=0}^{\infty}\sum_{m=-k}^{k} z_{km}(t)Y_k^m(\theta,\phi) \tag{17}$$

we have that

$$Z(\theta,\phi,t) = \sum_{k=0}^{\infty}\sum_{m=-k}^{k} Z_{km}(t)Y_k^m(\theta,\phi) \tag{18}$$

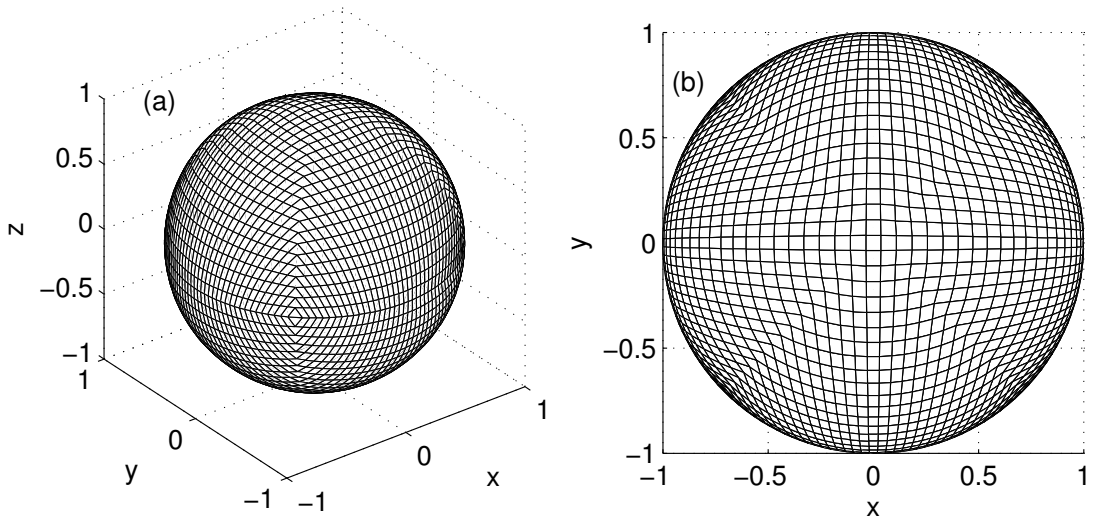

FIGURE 7. Spherical mesh used for the computations in Sec. 2.3, with $N = 40$. (b) shows the view from above.

where (see Appendix A)

$$Z_{km}(t) = z_{km}(t) b_k \sqrt{\frac{4\pi}{2k+1}} \tag{19}$$

and the b_k are given by (13). As in Sec. 2.2, we need to spatially discretise the domain, which is now the surface of the unit sphere. We use a scheme proposed in [8]. The computational domain is $\{(X, Y) : -3 \le X \le 1, -1 \le Y \le 1]\}$ which is uniformly discretised with $2N - 1$ points in X and N points in Y. Each point (X_i, Y_j), where $1 \le i \le 2N - 1$ and $1 \le j \le N$, is then mapped to a point (x_{ij}, y_{ij}, z_{ij}) in the surface of the unit sphere. We define $\theta_{ij} = \cos^{-1}(z_{ij})$ and $\phi_{ij} = \text{atan2}(y_{ij}, x_{ij})$, where $\text{atan2}(y, x)$ is the four-quadrant inverse tangent of y and x as implemented in Matlab. The Matlab code for generating the coordinates of these points is in Appendix B, and an example grid when $N = 40$ is shown in Fig. 7.

An alternative grid could involve equally-spaced discretisation in both θ and ϕ. While such a grid would enable straightforward evaluation of an integral like (67), needed to evaluate the $z_{km}(t)$ given $z(\theta, \phi, t)$, the density of points would be highly non-uniform, packed towards the poles and sparse at the equator, which we would like to avoid. In contrast, for the grid used here the ratio of largest to smallest grid cell is less than 2 [8]. In general there is no way to uniformly distribute an arbitrary number of points over a sphere; see [60, 49, 8] for more discussion on this topic.

As just alluded to, in order to calculate Z (the convolution of z with B) using (18) and (19) we must find the $z_{km}(t)$ given the values at the grid points, $z(\theta_{ij}, \phi_{ij}, t)$. In principle, one could use these values to approximate an integral like (67), but given the non-uniformity of points on the sphere doing this directly seems highly nontrivial. An alternative approach would be to interpolate the values $z(\theta_{ij}, \phi_{ij}, t)$ onto a regular polar grid, with equally-spaced discretisation in both θ and ϕ, and then use these values

to approximate an integral like (67), but we have not considered this here. Instead we will find the $z_{km}(t)$ which *best fit* the values $z(\theta_{ij},\phi_{ij},t)$. To do this we first truncate the sum over k in (17) and (18) at $k=M$, and evaluate (17) at the grid points to give

$$z(\theta_{ij},\phi_{ij},t)=\sum_{k=0}^{M}\sum_{m=-k}^{k}z_{km}(t)Y_k^m(\theta_{ij},\phi_{ij}) \tag{20}$$

for $i=1,2,\dots 2N-1$ and $j=1,2\dots N$, where we regard the $z(\theta_{ij},\phi_{ij},t)$ as knowns and the $z_{km}(t)$ as unknowns. If $(M+1)^2<(2N-1)N$, eqn. (20) is an overdetermined system with more equations than unknowns. We obtain the best fit solution of (20) by minimising the scalar quantity

$$\sum_{i=1}^{2N-1}\sum_{j=1}^{N}\left[z(\theta_{ij},\phi_{ij},t)-\sum_{k=0}^{M}\sum_{m=-k}^{k}z_{km}(t)Y_k^m(\theta_{ij},\phi_{ij})\right] \times\left[\overline{z}(\theta_{ij},\phi_{ij},t)-\sum_{k=0}^{M}\sum_{m=-k}^{k}\overline{z}_{km}(t)\overline{Y}_k^m(\theta_{ij},\phi_{ij})\right] \tag{21}$$

using linear least-squares. These values $z_{km}(t)$ are then used in (18) and (19) to evaluate $Z(\theta_{ij},\phi_{ij},t)$. Linear least-squares gives equal weight to each grid point, and this is a reason for choosing a relatively uniform grid on the sphere. The same technique is used to simulate the full network of phase oscillators (i.e. a spatial discretisation of (1)), the results of which are discussed in Sec. 5.

We always use the value $M=20$, and one might consider increasing this in order to better resolve the "fine structure" in $z(\theta,\phi)$ using higher harmonics. However, when calculating the convolution, one can see from (19) that coefficients corresponding to large k are multiplied by the corresponding b_k, and these decay with k (quickly for small κ and more slowly for larger κ) and thus increasing M leads to diminishing returns. This is just a manifestation of the well-known result that convolution is a smoothing operation, resulting in the reduction of "high frequency" components relative to more slowly varying ones.

2.3.1. *Numerical continuation.* A typical stationary spiral wave solution of (16) is shown in Figs. 8 and 9 ($\Omega\approx 0.43965$). For computational purposes, only the values of z in the left half of the computational domain (i.e. $-3\le X\le -1$, see Fig. 9) are calculated. When the values of z over the whole sphere are needed, the bottom and top halves are set to be reflections of one another through the equator, i.e. the solution for $-1\le X\le 1$ is obtained by relecting that for $-3\le X\le -1$ about $X=-1$.

Note that in Secs. 2.1 and 2.2 we set $\Delta=0.01$ as the level of heterogeneity, whereas here we use $\Delta=0.1$. We found that doing this was necessary in order for stability calculations and continuation algorithms to converge. One way of understanding this is to observe the complete set of eigenvalues associated with the linearisation about a spiral wave, and their relationship to the essential spectrum, as discussed in Appendix C.

Continuing the solution shown in Fig. 8 (although with reduced N, for computational efficiency) as α is varied we obtain Fig. 10. (Compare with Fig. 17 of [21] and Figs. 2 and 3 in [37].) Fig 11 shows two representative spirals from the family shown in Fig. 10. The stable spiral becomes unstable through Hopf bifurcations as α is either increased or decreased but can be followed to $\alpha=0$ and $\alpha\approx 1.35$, where it collides with the zero solution. (This collision can also be seen as a Hopf bifurcation of the uniform state, creating the spiral as α is decreased, as occurs in reaction-diffusion systems [54].) The rotation

speed, Ω, increases approximately linearly in α for small α, as was found analytically in [37] for identical oscillators and also observed in [21] for non-identical oscillators. As $\alpha \to \sim 1.35$, the incoherent regions grow (as in [49]) until the whole sphere is incoherent, when it coincides with the zero state. As $\alpha \to 0$, the incoherent cores shrink to points at both poles and the spiral arms "straighten," as in [37, 49]. Note that [49] had difficulty determining the stability of spiral chimeras for small α, when there were few oscillators in the incoherent core. One disadvantage of using heterogeneous oscillators, as we do here, is that there is no longer a clear boundary between coherent oscillators (with $|z| = 1$) and incoherent ones ($|z| < 1$). However, an advantage of using the continuum limit equations with a heterogeneous population is that $|z|$ is then a smooth function of space and as long as sufficiently many spatial points are used to approximate it, there is no longer the concern of having too few incoherent oscillators, as we do not work with individual oscillators.

We found that we could continue solutions from the curve in Fig. 10 as κ increased to $\kappa \approx 50$, unlike [49]. However, our numerical scheme will break down at some point, because as $\kappa \to \infty$, the b_k from (13) decay slower and slower in k, and thus more and more terms are needed in (20) (i.e. we need to increase M) to accurately evaluate the convolution (18). Also, we found that as $\kappa \to \infty$ the pitch of a spiral decreases, i.e. the spirals become more tightly wound (this was most pronounced for $\alpha \approx \pi/4$, where [49] had most difficulties) and thus more spherical harmonics are likely to be need to accurately describe the spirals.

Decreasing κ for solutions shown in Fig. 10 we found that the spirals all collide with the zero state at a non-zero value of κ. This value (and the rotational frequency of the spiral at this bifurcation) can be calculated by linearising (16) about the origin. The linearisation is

$$\frac{\partial q(\theta,\phi,t)}{\partial t} = -(\Delta - i\Omega)q(\theta,\phi,t) + e^{-i\alpha}Q(\theta,\phi,t)/2 \tag{22}$$

where we expand

$$q(\theta,\phi,t) = \sum_{k=0}^{\infty}\sum_{m=-k}^{k} q_{km}(t)Y_k^m(\theta,\phi) \tag{23}$$

and

$$Q(\theta,\phi,t) = \sum_{k=0}^{\infty}\sum_{m=-k}^{k} Q_{km}(t)Y_k^m(\theta,\phi) \tag{24}$$

in spherical harmonics, where

$$Q_{km}(t) = q_{km}(t)b_k\sqrt{\frac{4\pi}{2k+1}} \tag{25}$$

Letting $q_{km}(t) = \widehat{q}_{km}e^{\mu_{km}t}$ and using the expression for b_k we have

$$\mu_{km} = -(\Delta - i\Omega) + \frac{e^{-i\alpha}\sqrt{\pi\kappa/2}}{2\sinh\kappa}I_{k+1/2}(\kappa) \equiv \widehat{\mu}_k \tag{26}$$

independent of m. Now

$$\mathrm{Re}(\widehat{\mu}_k) = -\Delta + \frac{\cos\alpha\sqrt{\pi\kappa/2}}{2\sinh\kappa}I_{k+1/2}(\kappa) \tag{27}$$

Spiral waves of the type considered here have $|m| = 1$, as $\arg(z)$ varies by $\pm 2\pi$ along any path with constant θ. Since $I_{k+1/2}(\kappa)$ increases monotonically with k, the value of k for which $\widehat{\mu}_k$ has the largest

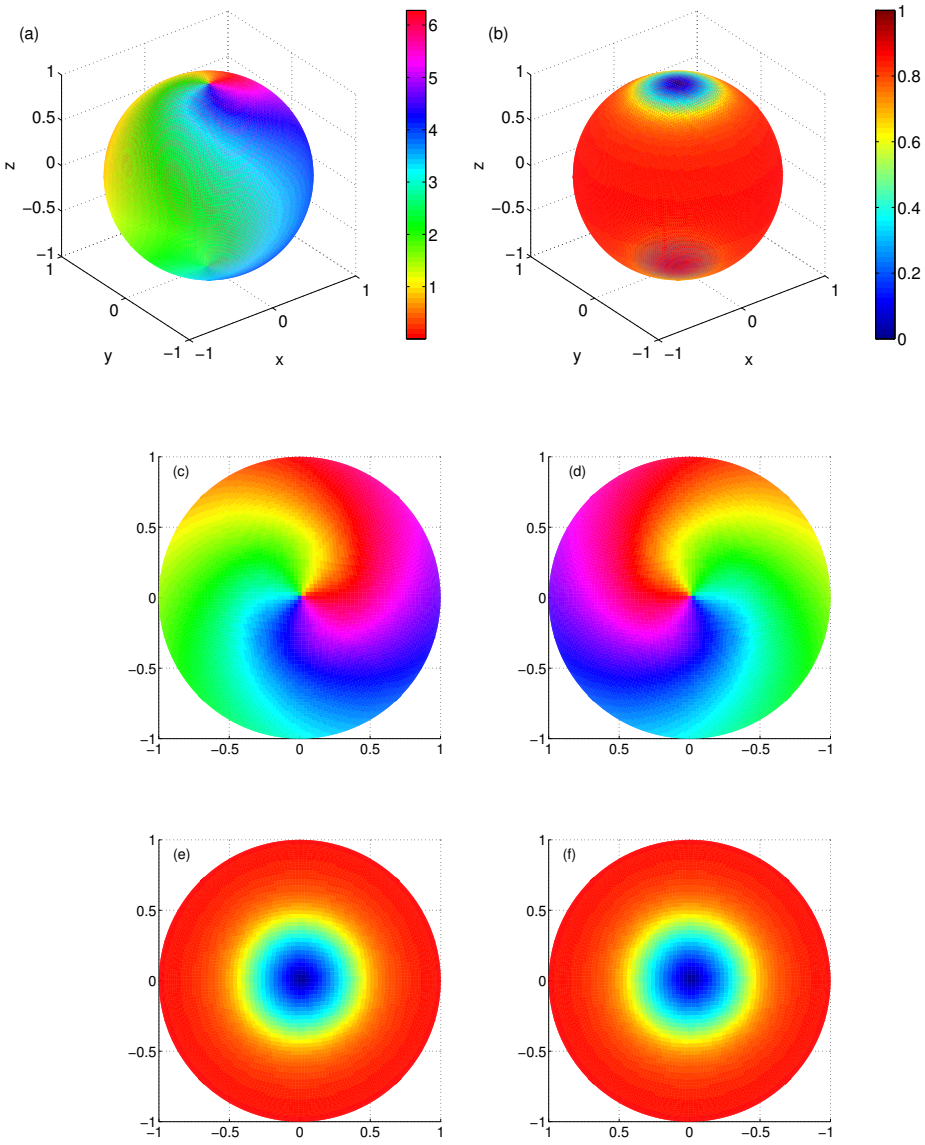

FIGURE 8. Typical spiral wave on a sphere. (a): $\arg(z)$. (b): $|z|$. (c) and (d): $\arg(z)$ seen from below and above, respectively (colours as in (a)). (e) and (f): $|z|$ seen from below and above, respectively (colours as in (b)). Note the reflection symmetry about the equator. Parameters: $N = 100, M = 20, \kappa = 10, \alpha = 0.66, \Delta = 0.1$.

real part (and which is consistent with $m = 1$) is $k = 1$, i.e. the spirals bifurcate from the zero state

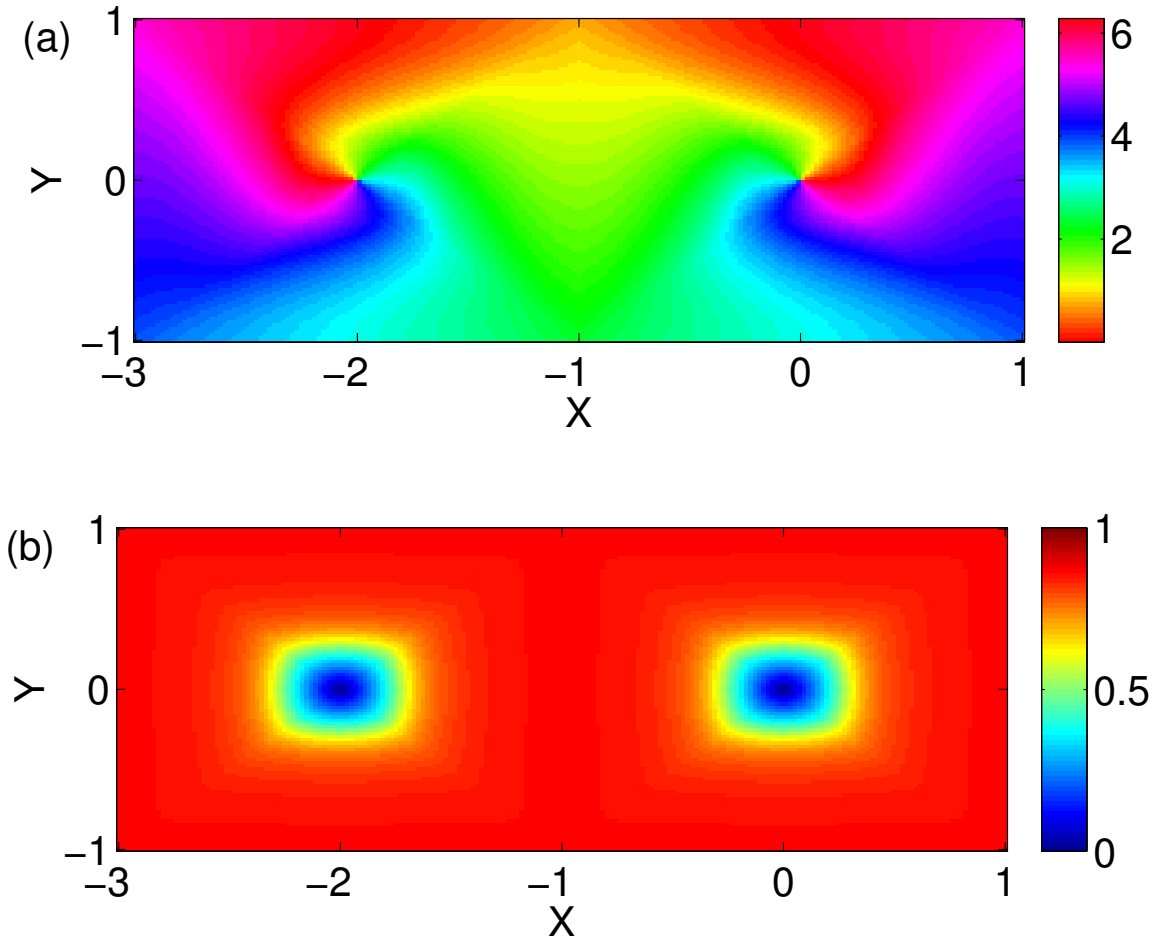

FIGURE 9. The solution shown in Fig. 8, shown in the computational domain: $(X, Y) \in [-3, 1] \times [-1, 1]$. (a): $\arg(z)$; (b): $|z|$. Note the reflection symmetry about $X = -1$.

when

$$\mathrm{Re}(\widehat{\mu}_1) = -\Delta + \frac{\cos\alpha\sqrt{\pi\kappa/2}}{2\sinh\kappa} I_{3/2}(\kappa) = 0 \tag{28}$$

(This curve is plotted dashed in Fig. 12.) We also have

$$\mathrm{Im}(\widehat{\mu}_k) = \Omega - \frac{\sin\alpha\sqrt{\pi\kappa/2}}{2\sinh\kappa} I_{k+1/2}(\kappa) \tag{29}$$

For the spiral to be stationary in a coordinate frame rotating with frequency Ω, we need $\mathrm{Im}(\widehat{\mu}_1) = 0$, i.e.

$$\Omega = \frac{\sin\alpha\sqrt{\pi\kappa/2}}{2\sinh\kappa} I_{3/2}(\kappa) \tag{30}$$

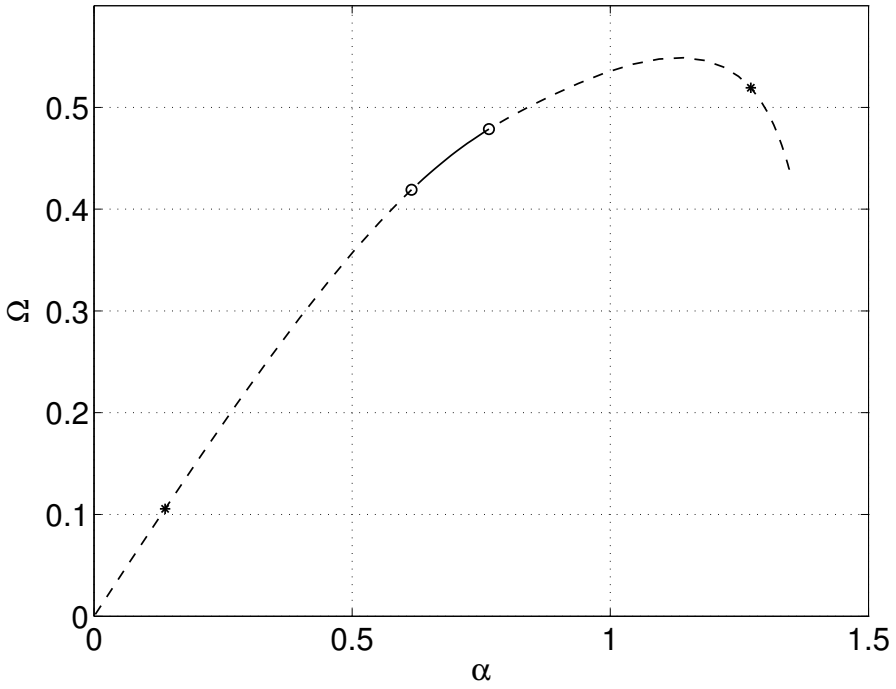

FIGURE 10. Continuation in α of the spiral wave shown in Fig. 8. Solid: stable; dashed: unstable. Two Hopf bifurcations are marked with circles. The right end of the curve corresponds to the spiral colliding with the zero solution. Solutions at the points marked with asterisks are shown in Fig. 11. Parameters: $N = 50, M = 20, \Delta = 0.1, \kappa = 10$.

where α and κ satisfy (28). So, for example, setting $\kappa = 10$ in (28) and solving for α, then putting these values into (30) we find that the curve in Fig. 10 terminates at $(\alpha, \Omega) = (1.3467, 0.43875)$ (5 significant figures).

Continuing the Hopf bifurcations shown in Fig. 10 as both α and κ are varied we obtain Fig. 12. We see that the two curves meet and cross, demarking a region labelled "A" in which the spiral waves studied here are stable. These results explain the observation by [49] that stable spiral chimeras only existed in a narrow strip, whose tip (for identical oscillators) was at $\alpha \approx 0.85$ and $\kappa \approx 8.5$.

2.3.2. *Other solutions.* The curve of Hopf bifurcations marking the left boundary of the region "A" in Fig. 12 is subcritical, and to the left of it the only stable solution seems to be the spatially uniform state, described by (9). The curve of Hopf bifurcations marking the right boundary of the region "A" seems to be supercritical, and an example of a pair of oscillating spirals emanating from this curve in shown in `hopfsph.avi`. This shows the solution in the computational domain $(X, Y) \in [-3, 1] \times [-1, 1]$. The top half shows $|z|$ and the bottom shows $\arg(z)/(2\pi)$, where $\arg(z)$ at $(X, Y) = (-3, -1)$, i.e. the bottom left corner, is always set to be zero. Parameter values are $\alpha = 0.7$ and $\kappa = 15$ (and $N = 80$). Red corresponds to 1 and blue to zero. (Note that the reflection symmetry about $X = -1$ is not imposed here, nor in the following movies.) Going further from this curve the pair of oscillating spiral cores seen

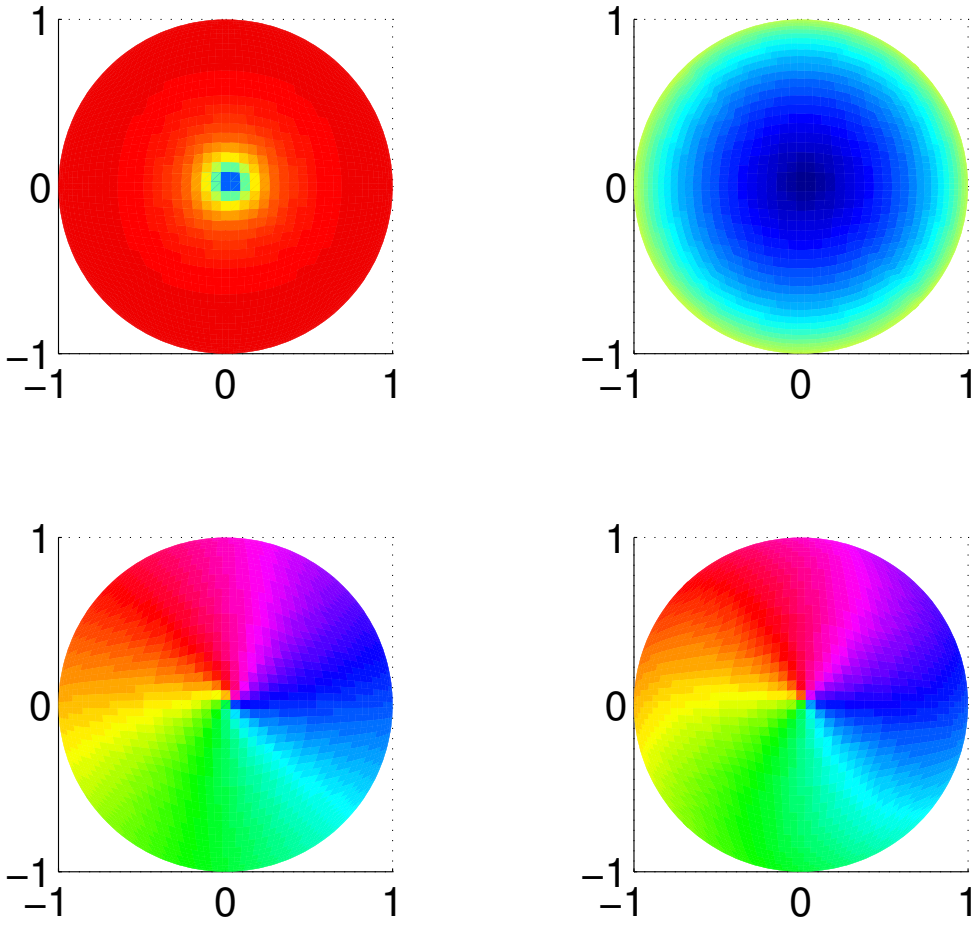

FIGURE 11. Two representative spirals (seen from below) from points marked with asterisks on the curve shown in Fig. 10. Top row: $|z|$ (blue= 0, red= 1). Bottom row: $\arg(z)$ (colours are as in Fig. 9 (a)). Left column: $\alpha = 0.13768$. Right column: $\alpha = 1.2721$. Other parameters: $N = 50, M = 20, \Delta = 0.1, \kappa = 10$.

in `hopfsph.avi` seem to become chaotic. An example is shown in `chaostwop.avi`, for parameter values $\alpha = 0.85$ and $\kappa = 17$ (and $N = 80$). Note that there are still two incoherent cores for this solution. There is also a range of parameter values $3 \lesssim \kappa$ and $1.1 \lesssim \alpha \lesssim 1.3$ for which spatiotemporally chaotic solutions are stable. An example is shown in the movie `chaossph.avi`, for $\alpha = 1.2$ and $\kappa = 5$ (and $N = 80$). Note that in contrast with the solution shown in `chaostwop.avi`, there are no incoherent cores which persist for all time.

A sweep over the parameter space shown in Fig. 12 with random initial conditions shows that apart from the solutions mentioned above, the only other type of stable solution is the spatially uniform state.

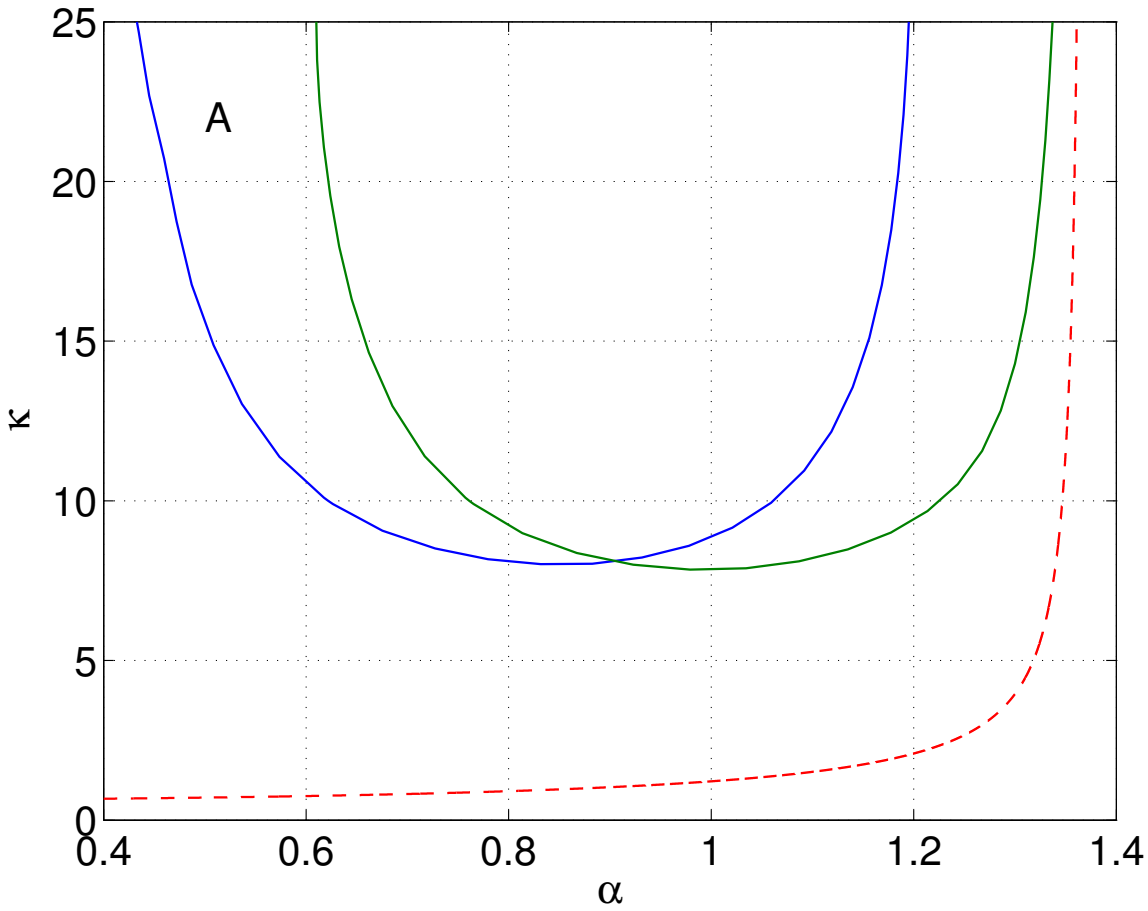

FIGURE 12. Continuation of Hopf bifurcations of spirals shown in Fig. 10 (solid) and the curve on which these spirals bifurcate off the zero state (eqn. (28), dashed). Spiral waves are only stable in the region marked "A". Fig. 10 corresponds to a horizontal "slice" through this Figure at $\kappa = 10$. (Note that the rightmost two Hopf bifurcations are not shown in Fig. 10.) Other parameters: $N = 50, M = 20, \Delta = 0.1$.

In summary, we have resolved a number of issues that arose in the original study of oscillators on a sphere [49], perhaps the most significant being the determination of the boundaries of stability (corresponding to Hopf bifurcations) of the spiral chimeras (Fig. 12).

3. Two-dimensional flat torus with D_4-symmetric coupling

Here we re-examine the results of Xie et al. [66], who considered a system whose continuous version can be written

$$\frac{\partial\theta(x,y,t)}{\partial t} = \omega(x,y) - \int_{-\pi}^{\pi}\int_{-\pi}^{\pi} G(x-x',y-y')\sin\left[\theta(x,y,t) - \theta(x',y',t) + \alpha\right]dx'dy' \tag{31}$$

with periodic boundary conditions in x and y, i.e. the domain is a flat two-torus. These authors set $\omega(x,y)=0$ and considered several forms of coupling, among which were

$$G_1(x,y)=\cos x+\cos y \tag{32}$$

and

$$G_2(x,y)=\cos x+\cos(2x)+\cos y+\cos(2y) \tag{33}$$

Note that the domain is a square and these coupling functions have D_4 symmetry. Xie et al. found a variety of states whose existence and stability could be described analytically, and we will not discuss most of them. However, they found one particularly interesting state for coupling G_2, in which spiral wave chimeras have partially or intermittently incoherent cores, unlike those observed in [49, 44, 37, 21]. The authors noted that in the work of others, such "crescent structures" were associated with the onset of a core instability, but no such instability was found for coupling G_2.

Here we consider the coupling

$$G(x,y;\lambda)=\cos x+\cos y+\lambda[\cos(2x)+\cos(2y)] \tag{34}$$

so that $G(x,y;0)=G_1(x,y)$ and $G(x,y;1)=G_2(x,y)$. By varying λ from 0 to 1 we can interpolate between $G=G_1$ and $G=G_2$.

Choosing the $\omega(x,y)$ from a Lorentzian with mean zero and halfwidth Δ, using the Ott/Antonsen ansatz, and moving to a rotating coordinate frame we derive the equivalent evolution equation

$$\frac{\partial z(x,y,t)}{\partial t}=-(\Delta-i\Omega)z(x,y,t)+e^{-i\alpha}Z(x,y,t)/2-e^{i\alpha}z^2(x,y,t)\overline{Z}(x,y,t)/2 \tag{35}$$

where

$$Z(x,y,t)=\int_{-\pi}^{\pi}\int_{-\pi}^{\pi}G(x-x',y-y';\lambda)z(x',y',t)dx'\ dy' \tag{36}$$

Note that the coupling function G is balanced, in the sense that

$$\int_{-\pi}^{\pi}\int_{-\pi}^{\pi}G(x-x',y-y';\lambda)dx'\ dy'=0 \tag{37}$$

Thus the only spatially-uniform state is $z=0$.

A typical steady state of (35) is shown in Fig. 13 ($\Omega\approx 9.6042$). We discretised the domain using a regular $N\times N$ cartesian grid and approximated the spatial convolutions using the Fast Fourier Transform. The solution in the upper left corner can be obtained by reflecting that in the upper right corner in the y-axis, and the solution for $y<0$ is obtained by reflecting the solution for $y>0$ in the x-axis. Thus for computational purposes we only work with the solution on $[0,\pi]\times[0,\pi]$, forming the rest as required using the reflections just mentioned. Note that the heterogeneity level is $\Delta=0.1$, the same value as used in Sec. 2.3.1

3.1. **Numerical continuation.** We show in Appendix D that steady states of (35) are independent of λ. However, their stability does depend on λ. We choose three representative values of α, find stable steady states of (35) when $\lambda=0$ for these values of α, and then determine the stability of these solutions as a function of λ. The three values are $\alpha=\pi/2-0.4,\pi/2-0.6$ and $\pi/2-1.2$, and the corresponding steady states are shown in Fig. 14. (Only the top right quarter of the domain is shown.) We find that for $\alpha=\pi/2-0.4$, the solution is stable for $0\le\lambda<0.92096$ and unstable for larger values of λ. The instability is a Hopf bifurcation. For $\alpha=\pi/2-0.6$, the solution is stable for all $0\le\lambda\le 1$.

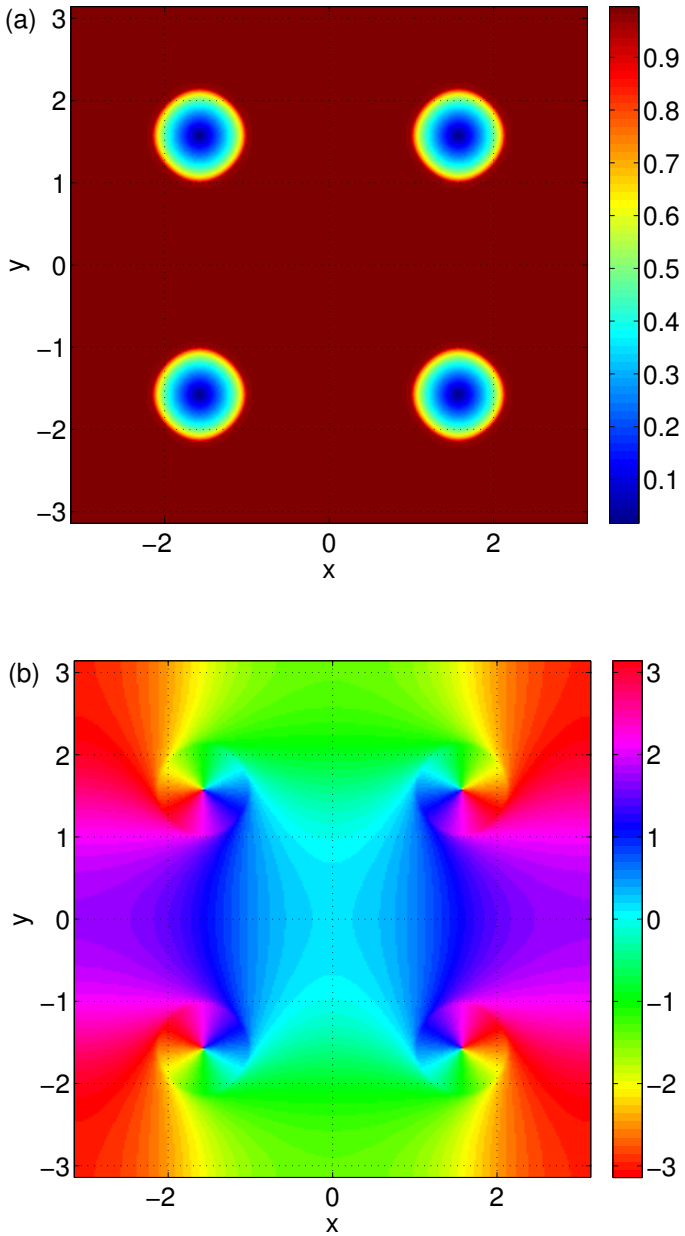

FIGURE 13. Stable steady state of (35). (a): $|z|$; (b): $\arg(z)$. Parameters: $\lambda = 0, N = 256, \Delta = 0.1, \alpha = \pi/2 - 1$.

For $\alpha = \pi/2 - 1.2$, the solution is stable for $0 \leq \lambda < 0.9746$ and unstable for larger values; again, the instability is a Hopf bifurcation. (Results were verified with $N = 512$.) Snapshots of the dynamic states after the Hopf bifurcations, when $\lambda = 1$, are shown in Fig. 15 and corresponding movies are `hopf4.avi`

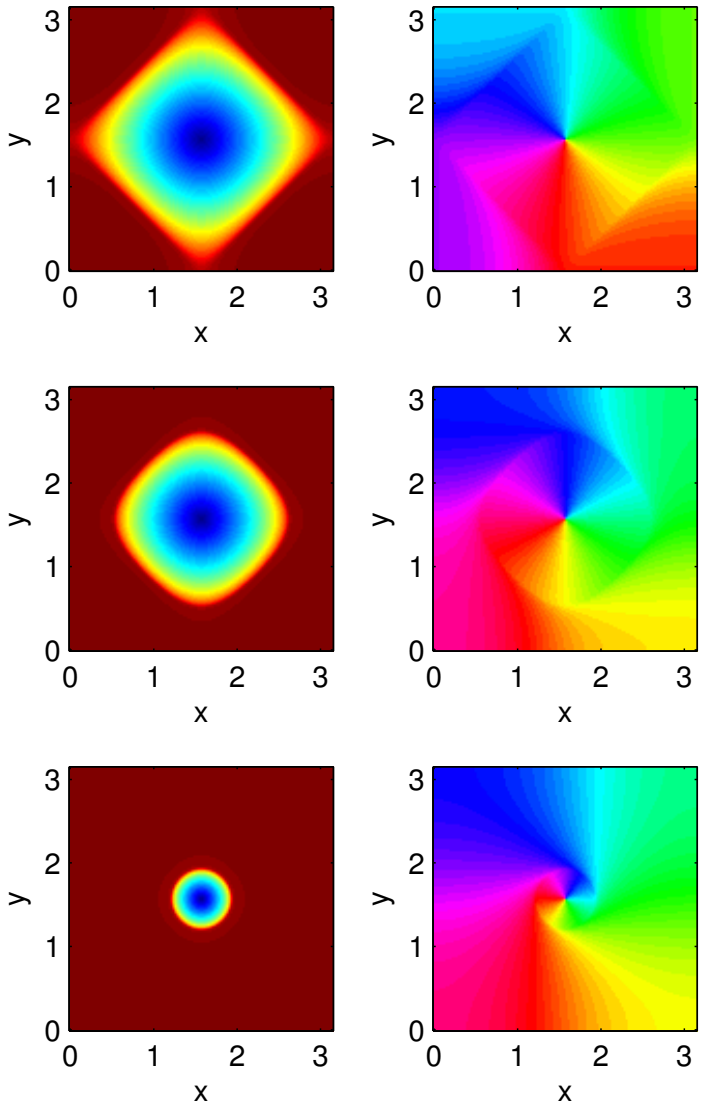

FIGURE 14. Stable steady states of (35) (only the top right quarter of the domain is shown). Top row: $\alpha = \pi/2 - 0.4$ ($\Omega = 14.988$); middle row: $\alpha = \pi/2 - 0.6$ ($\Omega = 14.119$); bottom row: $\alpha = \pi/2 - 1.2$ ($\Omega = 6.497$). Left column: $|z|$ (blue is 0, red is 1). Right column: $\arg(z)$ (colours are as in Fig. 9 (a)). Parameters: $\lambda = 0, N = 256, \Delta = 0.1$.

($\alpha = \pi/2 - 0.4$) and `hopf12.avi` ($\alpha = \pi/2 - 1.2$). These states look very similar to those observed by [66] for coupling function G_2 (i.e. our coupling function (34) with $\lambda = 1$).

From quasi-statically varing λ it seems that the Hopf bifurcation for $\alpha = \pi/2 - 0.4$ mentioned above is supercritical, while that for $\alpha = \pi/2 - 1.2$ is slightly subcritical, with an unstable branch of oscillatory

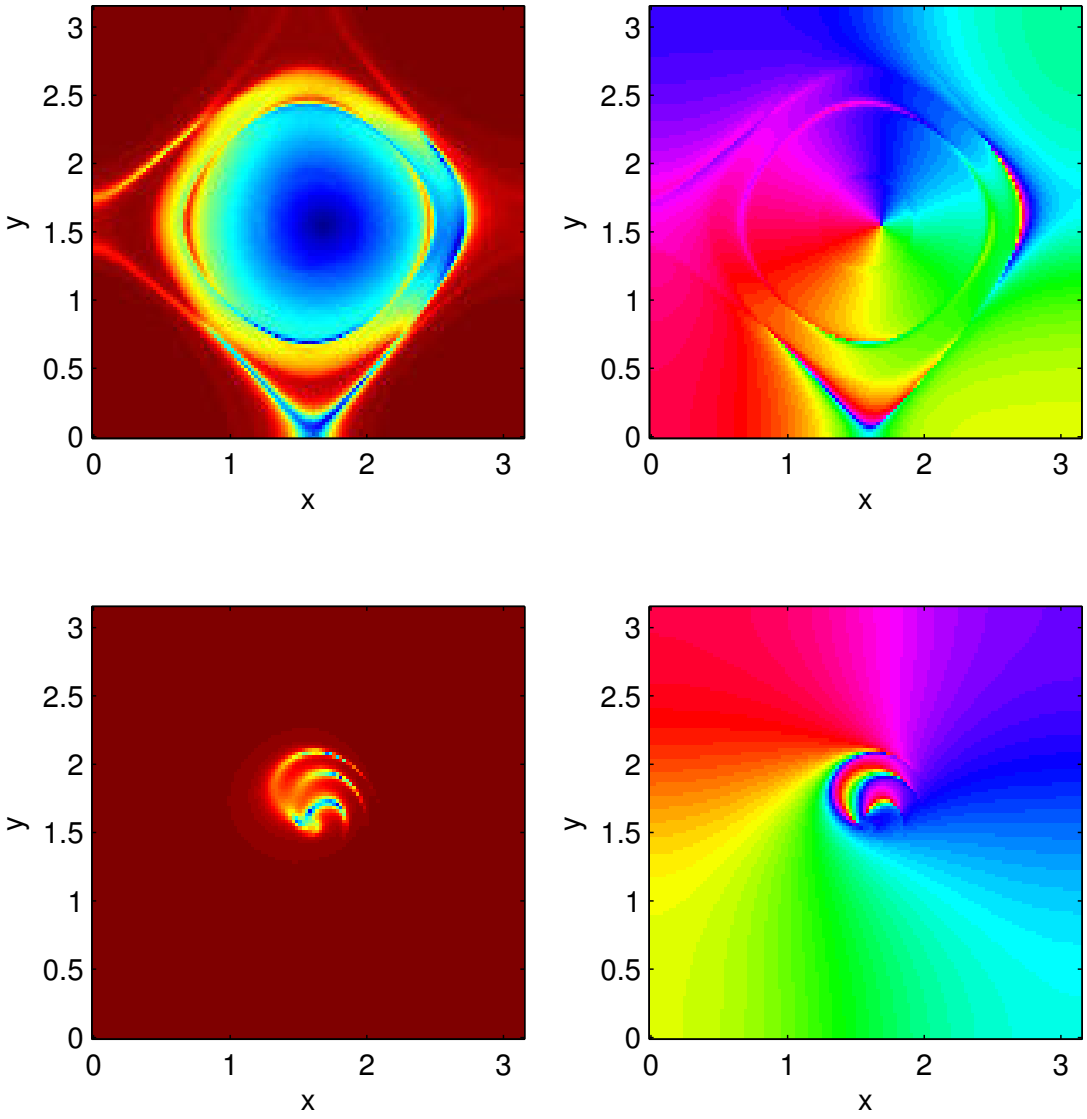

FIGURE 15. Snapshots of dynamic states of (35) with $\Omega = 0$ and $\lambda = 1$ (only the top right quarter of the domain is shown). Top row: $\alpha = \pi/2 - 0.4$; bottom row: $\alpha = \pi/2 - 1.2$. Left column: $|z|$ (blue is 0, red is 1). Right column: $\arg(z)$ (colours are as in Fig. 9 (a)). Other parameters: $N = 256, \Delta = 0.1$.

solutions created from the bifurcation as λ is decreased, and a small corresponding window of bistability between stationary and oscillatory states. However, it does seem clear that the oscillatory solutions shown in Fig. 15 result from Hopf bifurcations of the solutions shown in Fig. 14 as λ is increased. And while our solutions cannot be directly compared with those of [66] due to the heterogeneity of oscillator

frequencies in (31), it seems likely that the "crescent structures" they observed with coupling G_2 also arise from Hopf bifurcations of the solutions they found for coupling G_1, as ours do.

4. Two-dimensional flat torus with circular neighbourhood

We now consider a network similar to that studied by Omel'chenko et al. [44]. These authors considered a network of identical phase oscillators on a regular $N \times N$ array which evolve according to

$$\frac{d\Psi_{jk}}{dt} = \omega - \frac{1}{|B_R(j,k)|} \sum_{(m,n)\in B_R(j,k)} \sin\left(\Psi_{jk} - \Psi_{mn} + \alpha\right) \tag{38}$$

where R is coupling range and the neighbourhood of the point (j,k) is

$$B_R(j,k) = \{(m,n) : \sqrt{(m-j)^2 + (n-k)^2} \le R\} \tag{39}$$

and all indices are calculated using periodic boundary conditions in both directions (i.e. the domain is a flat torus). They found coherent and incoherent spot solutions, as well as stripe and spiral chimeras.

We consider a slight modification of their model, given by

$$\frac{d\Psi_{jk}}{dt} = \omega_{jk} - \frac{1}{K} \sum_{m=1}^{N} \sum_{n=1}^{N} f\left[(2/N)\sqrt{(m-j)^2 + (n-k)^2} - h\right] \sin\left(\Psi_{jk} - \Psi_{mn} + \alpha\right) \tag{40}$$

also with periodic boundary conditions, where the decreasing function f is given by $f(r) = [1 + \tanh(-\gamma r)]/2$ and the normalisation factor K is

$$K \equiv \sum_{m=1}^{N} \sum_{n=1}^{N} f\left[(2/N)\sqrt{(m-j)^2 + (n-k)^2} - h\right] \tag{41}$$

(which is independent of j and k). Setting all $\omega_{jk} = \omega$ and letting $\gamma \to \infty$ we obtain (38), with $R = hN/2$ (thus the largest value of R considered by [44], $N/2$, corresponds to $h = 1$). We choose the ω_{jk} independently from a Lorentzian with mean zero and half-width Δ, in order that the Ott/Antonsen ansatz be valid. We fix $\gamma = 100$; the reason for having finite γ is that we want to use the coupling radius as a continuous parameter, so that solutions can be continued as it is varied, and when using a neighbourhood of the form (39) the number of grid points in the neighbourhood is a discontinuous function of R.

Using the Ott/Antonsen ansatz and moving to a rotating coordinate frame we derive the equivalent evolution equation

$$\frac{\partial z_{jk}(t)}{\partial t} = -(\Delta - i\Omega) z_{jk}(t) + e^{-i\alpha} Z_{jk}(t)/2 - e^{i\alpha} z_{jk}^2(t) \overline{Z}_{jk}(t)/2 \tag{42}$$

where

$$Z_{jk}(t) = \frac{1}{K} \sum_{m=1}^{N} \sum_{n=1}^{N} f\left[(2/N)\sqrt{(m-j)^2 + (n-k)^2} - h\right] z_{mn}(t) \tag{43}$$

Strictly speaking, to derive (42) we have not taken the limit of an infinite number of oscillators, but rather an infinite ensemble of networks with the same connectivity, all with different realisations of the ω_{jk}, as in [29, 6].

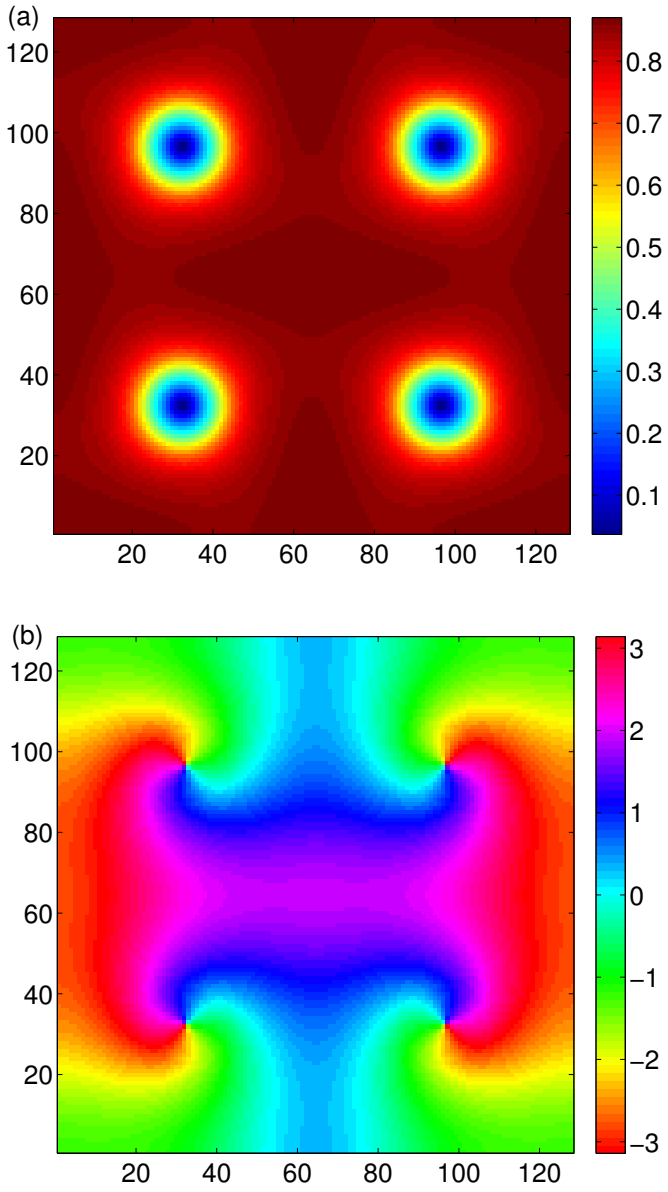

FIGURE 16. Stable steady state of (42). (a): $|z|$; (b): $\arg(z)$. Parameters: $h = 0.22, N = 128, \Delta = 0.1, \alpha = 0.7$.

4.1. **Spiral waves.** An example of a stable spiral wave is shown in Fig. 16. As for the model studied in Sec. 3, periodic boundary conditions mean that a single spiral wave cannot be supported; the smallest number that appear in a stable configuration is 4. As in Sec. 3, we impose that the solution be invariant under reflection about the vertical and horizontal midlines of the domain, and only compute with the solution in one quadrant.

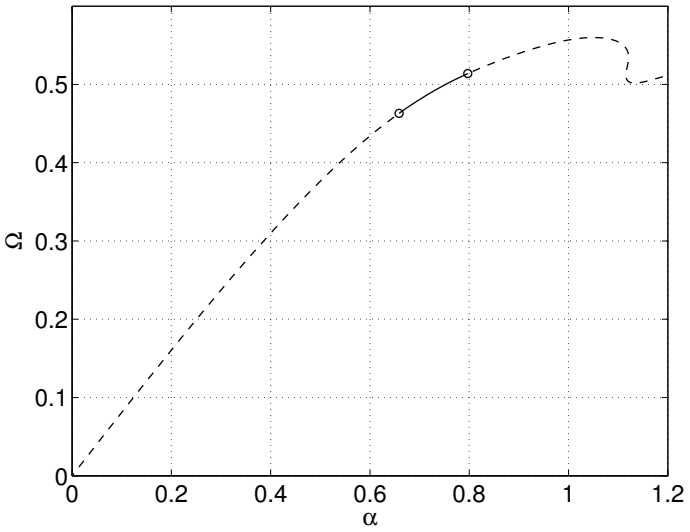

FIGURE 17. Rotation speed Ω as a function of α for the spiral wave shown in Fig. 16. Solid: stable; dashed: unstable. Two Hopf bifurcations are shown with circles. Other parameters: $h = 0.22, N = 128, \Delta = 0.1$.

Following the solution in Fig. 16 as α is varied we obtain Fig. 17. As in Sec. 2.3.1, we find that the spiral wave is stable over a small interval of α values, even though it exists over a much wider range. Both instabilities are Hopf bifurcations. As in Sec. 2.3.1, the spiral arms straighten and the incoherent core shrinks as $\alpha \to 0$. However, unlike in Sec. 2.3.1, the curve of spirals does not terminate for large α with a collision with the zero state, but rather the solutions become less spiral-like and eventually the continuation algorithm breaks down, without the solutions ever becoming stable again.

Following the Hopf bifurcations shown in Fig. 17 we obtain Fig. 18. As for the solutions in Sec. 2.3, we find the spiral waves to be stable in a "wedge" in parameter space, marked "A", in good agreement with the results of [44]. Compare Fig. 18 with Fig. 12, recalling that increasing κ is equivalent to decreasing h, in the sense of localising the spatial coupling. The criticality of the Hopf bifurcations marking the boundary of the region of stable spiral waves, and the behaviour beyond them, are the same as in Sec. 2.3.1. The lower Hopf curve in Fig. 18 seems subcritical, and below it the only attractor is the spatially-uniform state. The curve marking the upper boundary of region "A" seems supercritical, with stable oscillatory spirals just above it, and chaotic solutions for larger α.

4.2. **Stripes and Spots.** "Stripe" chimera solutions have no dependence on one of the coordinate directions and are thus effectively one-dimensional; see Fig. 19 for an example. At least in terms of existence, their behaviour should be similar to that of the single spot solution studied in Sec. 2.2, and the chimeras studied on a ring of oscillators [3, 21, 20, 18, 2, 64, 42]. Following a stripe chimera as α is varied we obtain the red curve in Fig. 20 (compare with Fig. 3). The stable stripe is destroyed in a saddle-node bifurcation as α is decreased and loses stability as α is increased in a symmetry-breaking bifurcation (unlike the stripe solution, the eigenvector associated with the zero eigenvalue at this bifurcation is not invariant under horizontal shifts). This is in contrast with the spot solution

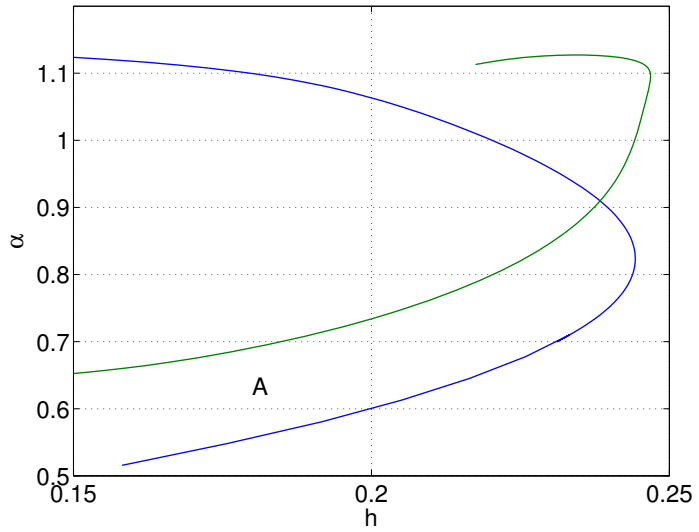

FIGURE 18. Curves of Hopf bifurcations of the spiral wave shown in Fig. 16. The spiral is stable in the region marked "A". The curves terminate where the numerical continuation algorithm broke down. Other parameters: $N = 128, \Delta = 0.1$.

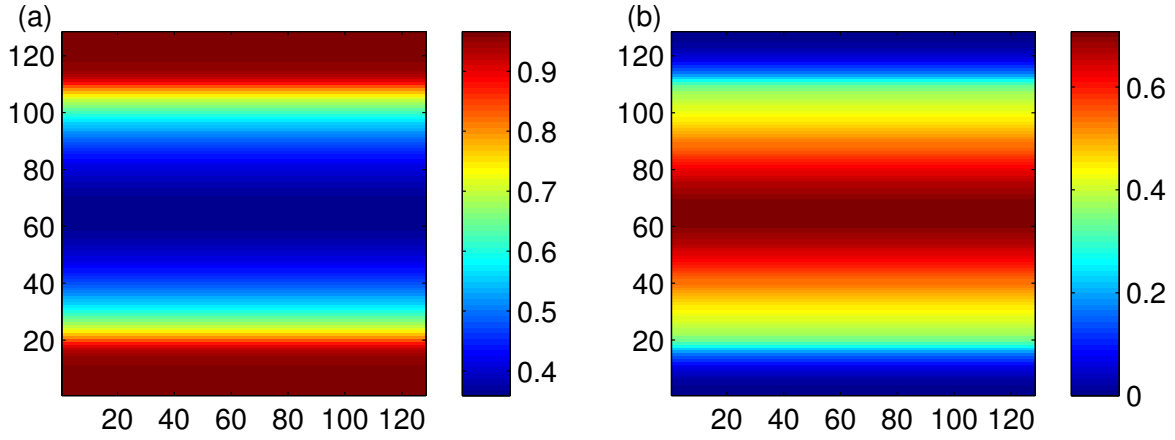

FIGURE 19. A typical stable stripe solution. (a) $|z|$; (b) $\arg(z)$. Other parameters: $h = 0.7, \alpha = 1.4, N = 128, \Delta = 0.01$.

whose behaviour is shown in Fig. 3, in which the spot loses stability through a Hopf bifurcation as α is increased. However, the two cases cannot be compared exactly, as the results shown in Fig. 3 do not consider perturbations which break the rotational invariance of the underlying spot solution (and the domain in Sec. 2 is a sphere, not a flat torus). As in Fig. 3, the branch of stripe solutions terminates in collisions with the spatially uniform state.

The authors [44] distinguished between coherent spot chimeras and incoherent spot chimeras, for which most of the domain was either incoherent or coherent, respectively. However, from following

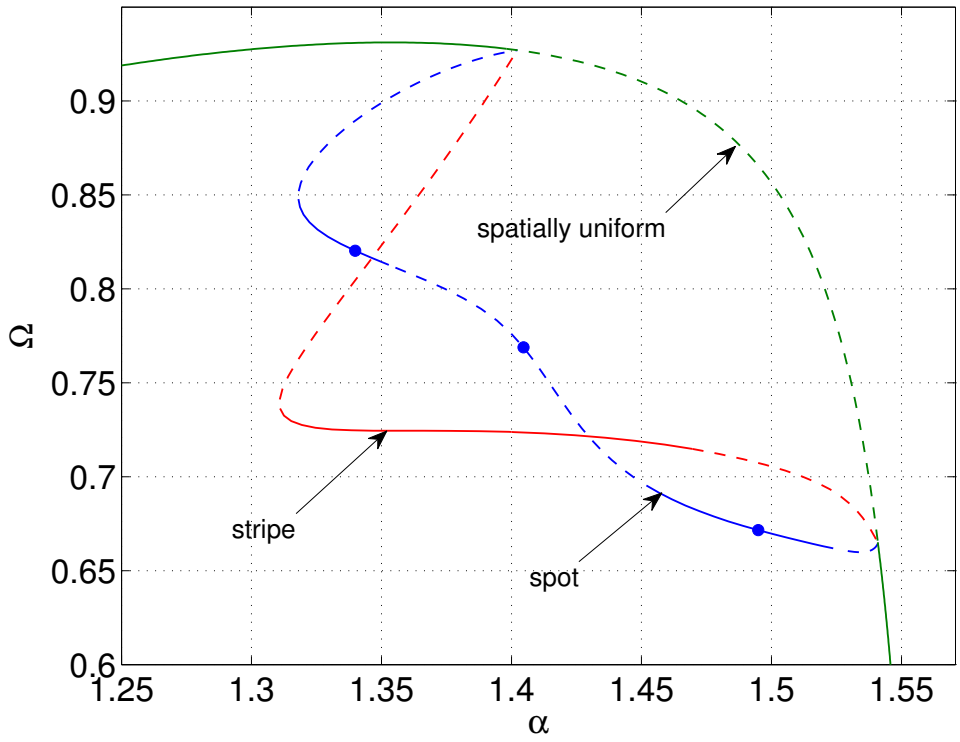

FIGURE 20. Ω as a function of α for the spatially uniform state (green), stripe chimeras (red), and spot chimeras (blue). Solid: stable, dashed: unstable. Solutions at the three points marked with solid circles are shown in Fig. 21. Other parameters: $h = 0.7, N = 128, \Delta = 0.01$.

these types of solutions we see that they form one family of solutions, as shown in Figs. 20 and 21. The only difference between them is the ratio of coherent to incoherent oscillators, which varies as a function of α. A similar observation was made by [47] for the case of identical oscillators.

Spot solutions are invariant under reflection in both the horizontal and vertical midlines (i.e. the symmetries imposed numerically), as well as rotation through $\pi/2$ about the centre of the domain. Consider the rightmost branch of stable spots in Fig. 20 (coherent spots). These solutions go unstable as α is increased through a Hopf bifurcation and then briefly become stable just before the branch collides with the spatially uniform state. (This change is not visible in Fig. 20, due to the scale used.) Decreasing α, the solutions lose stability to a symmetry-breaking bifurcation (the eigenvector associated with the zero eigenvalue is not invariant under a rotation through $\pi/2$ about the centre of the domain). Now consider the left-most branch of stable spots in Fig. 20 (incoherent spots). They are destroyed in a saddle-node bifurcation as α is decreased, and in a symmetry-breaking bifurcation as α is increased. The branch of spot solutions terminates by colliding with the spatially uniform state, at the same parameters as does the stripe solution. These bifurcations from the spatially uniform state could be understood using equivariant bifurcation theory [11] which takes into account the D_2 $(= Z_2 \times Z_2)$

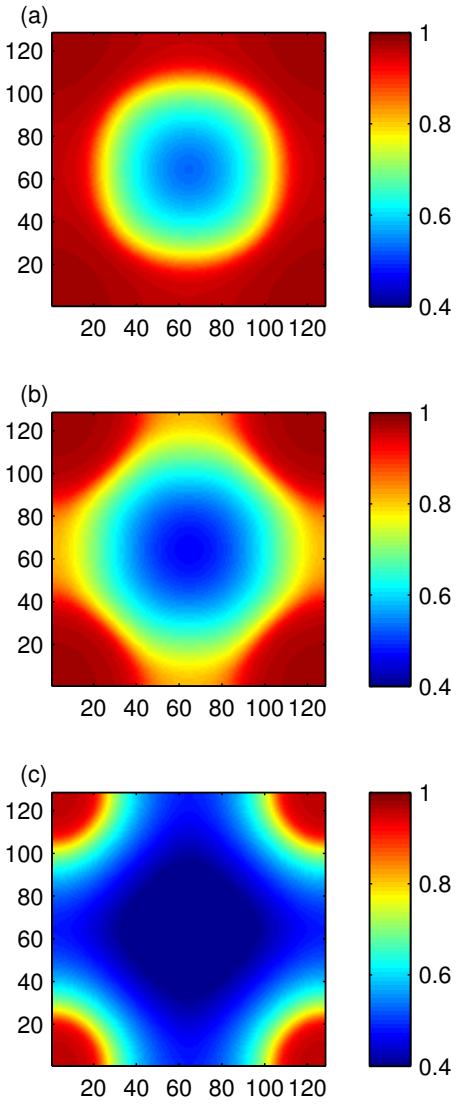

FIGURE 21. $|z|$ at the three points marked with filled circles in Fig. 20. (a) $\alpha = 1.3399$; (b) $\alpha = 1.4046$; (c) $\alpha = 1.4949$. Panel (a) shows a stable incoherent spot, while (c) shows a stable coherent spot (recall that the domain is periodic in horizontal and vertical directions). Panel (b) shows an unstable intermediate state. Other parameters: $h = 0.7, N = 128, \Delta = 0.01$.

symmetry imposed by the numerical scheme and the square symmetry of the computational domain, but we do not pursue that here.

Continuing the bifurcations seen in Fig. 20 as both h and α are varied we obtain Fig. 22. In the course of these continuations we found several other bifurcations (all Hopf bifurcations) which are not present in Fig. 20 (i.e. at $h = 0.7$) but are shown in Fig. 22. The bifurcation curves in Fig. 22 were continued beyond the values shown, but for simplicity we have shown only those curves corresponding to

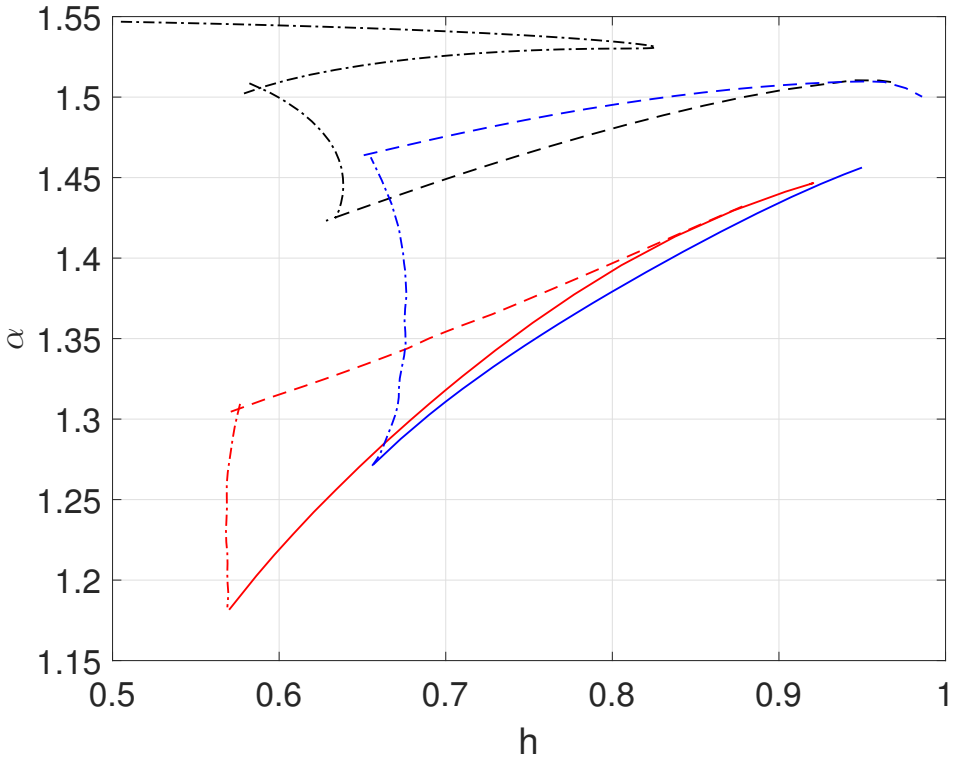

FIGURE 22. Bifurcation curves corresponding to the loss of stability of "incoherent spots" (red), stripes (blue), and "coherent spots" (black). Roughly speaking, these solutions are stable within the regions bounded by the curves of the corresponding colour. Solid: saddle-node bifurcation, dashed: symmetry-breaking bifurcation, dash-dotted: Hopf bifurcation. Fig. 20 corresponds to a vertical "slice" through this figure at $h = 0.7$. Other parameters: $N = 96, \Delta = 0.01$.

a loss of stability of a stable solution. Several of the curves terminated for $h \approx 1$ when the continuation algorithm broke down. (Recall that as $h \to 1$ the coupling kernel starts to "overlap" itself.) The results in Fig. 22 agree well with those of [44] and provide an explanation as to why these authors observed the sequence "incoherent spots — stripes — coherent spots" as α was increased for a fixed coupling kernel, and regions of bistability between these patterns.

A parameter sweep over $(h, \alpha) \in (0.01, 0.9) \times (0.01, 1.56)$ with random initial conditions and $\Delta = 0.01$ found that apart from the spirals, spots and stripes already found, the spatially uniform state was stable, along with multiple stripe and multiple spot solutions around $(h, \alpha) \approx (0.3, 1.3)$ (see, for example, the top row of Fig. 23), and spatially-disordered solutions for $\alpha \gtrsim 1.3$, particularly for small h (see, for example, the bottom row of Fig. 23).

5. DISCUSSION

In this paper we have reconsidered three previously-studied two-dimensional networks of phase oscillators known to support solutions such as spot, stripe and spiral chimeras [66, 49, 44]. By taking the

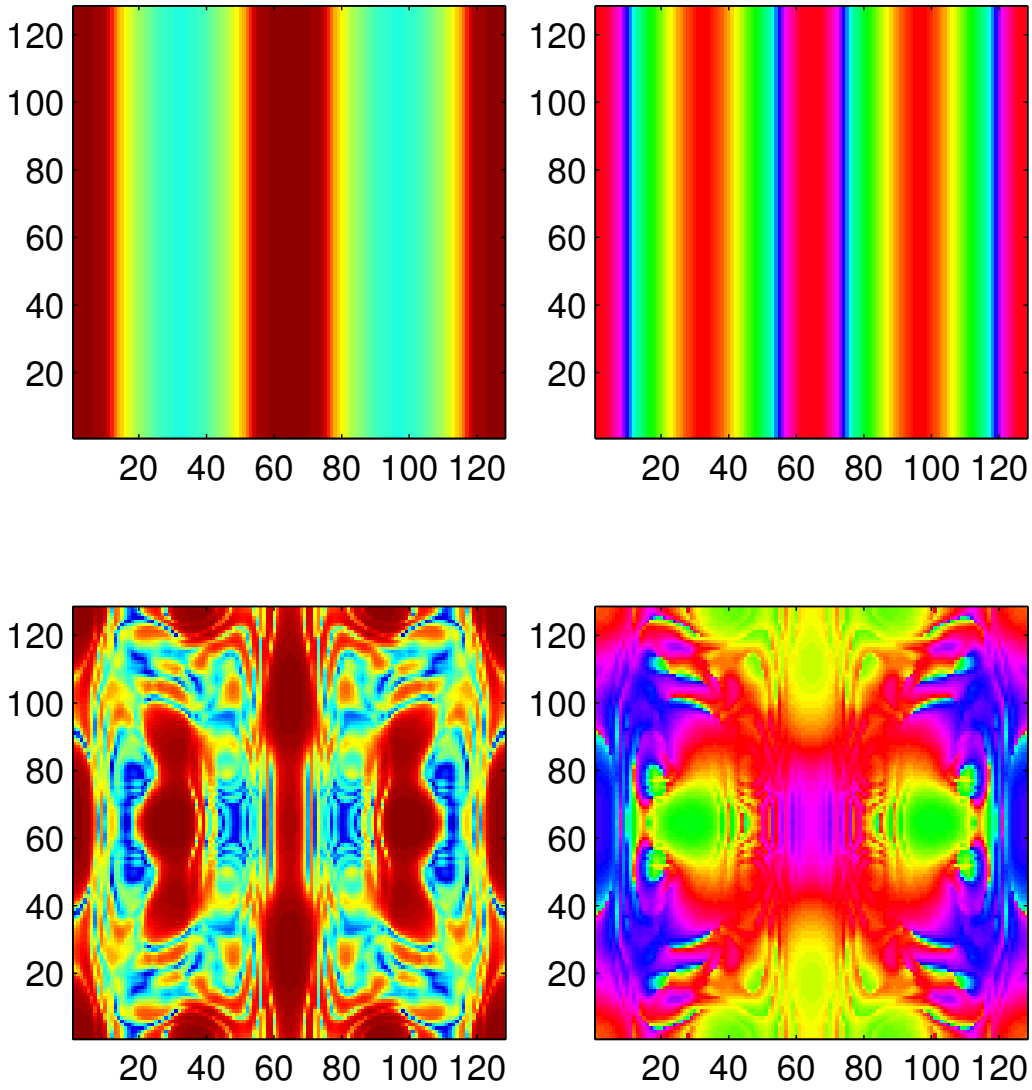

FIGURE 23. Snapshots of solutions of (42). The whole domain is shown (recall that we numerically impose that the solution is invariant under refection in the horizontal and vertical midlines). Top row: $h = 0.35$; bottom row: $h = 0.2$. Left column: $|z|$ (blue is 0, red is 1). Right column: $\arg(z)$ (colours are as in Fig. 9 (a)). Other parameters: $\alpha = 1.35, N = 128, \Delta = 0.01$.

continuum limit and using heterogeneous oscillators we used the Ott/Antonsen ansatz to derive continuum level evolution equations describing the networks' dynamics. Most of the solutions of interest are steady states of these evolution equations and we have shown the results of extensive numerical investigations of these equations. In particular, we have shown that the instabilities of spiral wave

chimeras in [49, 44] are very likely to be Hopf bifurcations (we cannot be completely sure, as we consider heterogeneous networks, while these authors considered networks of identical oscillators). We have also determined the bifurcations by which spot and stripe chimeras like those in [44] lose stability and provided strong evidence that the "crescent structures" observed by [66] in the cores of spiral wave chimeras do arise in Hopf bifurcations of rigidly rotating spirals. While we have concentrated solely on analysing the continuum limit equations, we have reproduced states equivalent to those shown in Figs. 8, 14, 15, 16, 19 and 21 by simulating the corresponding phase oscillator networks (results not shown).

We have not been able to compare our results directly with those of [66, 49, 44], who all considered networks of identical oscillators, due to the presence of purely imaginary spectra in the linearisation about a fixed point for such problems [64, 42]; this is incompatible with standard numerical bifurcation algorithms. However, computations like those presented here could be repeated for several different values of heterogeneity and the results extrapolated to the homogeneous case, in order for a comparison to be made.

We emphasise that our results are all numerical, and techniques used in analysing spiral waves in systems with diffusive coupling [54, 53] may shed light on the dynamics of spiral waves seen here. One interesting question unlikely to be answered with just computations is: why are spiral wave chimeras only stable for small α and localised coupling (see Figs. 12 and 18) whereas spot and stripe chimeras are only stable for α near $\pi/2$ and near-global coupling (see Figs. 4 and 22)?

We now mention several possible further applications of the framework presented here.

- Although we have only discussed systems with nonlocal coupling, it has recently been found that systems with just local coupling can also support chimera states [27, 32]. A self-consistency derivation of the form in [27] may be possible for spiral waves in locally coupled two-dimensional networks, and solutions of the resulting self-consistency equation might be followed using the same techniques used in this paper.
- Several recent papers show chimera states in simulations of three-dimensional networks of phase oscillators [34, 30]. The same techniques used here could be used to derive the corresponding three-dimensional evolution equations (assuming heterogeneous oscillators) which would describe these states. Although computationally challenging, this would put on firm ground statements regarding the stability or otherwise of solutions found in [34, 30], and their bifurcations.
- Two-dimensional networks of phase oscillators coupled by a delayed non-local mean field have interesting stable solutions such as spots, spirals and target patterns [23, 31]. The bifurcations of such patterns have (to our knowledge) not been studied.
- Heterogeneous networks of "theta neurons" and "Winfree oscillators" can be studied using the techniques presented here [51, 25, 33, 28, 9], however, the dynamics of two-dimensional networks of such oscillators also remains unstudied.

Acknowledgements: I thank Mark Panaggio, Edgar Knobloch and Oleh Omel'chenko for comments on the manuscript.

Appendix A. Convolutions on a sphere

We write a general function on the unit sphere in terms of spherical harmonics:

$$H(\theta,\phi)=\sum_{k=0}^{\infty}\sum_{m=-k}^{k}H_{km}Y_k^m(\theta,\phi) \tag{44}$$

where

$$Y_k^m(\theta,\phi)=\sqrt{\frac{(2k+1)}{4\pi}\frac{(k-m)!}{(k+m)!}}P_k^m(\cos\theta)e^{im\phi} \tag{45}$$

and P_k^m is the associated Legendre polynomial of degree k and order m. A circularly symmetric function can be written

$$B(\theta)=\sum_{l=0}^{\infty}\sqrt{\frac{2l+1}{4\pi}}b_lP_l(\cos\theta) \tag{46}$$

where P_l is the lth Legendre polynomial. The convolution of $B(\theta)$ with a general function $H(\theta,\phi)$ is

$$A(\theta,\phi)=\int_0^{\pi}\int_0^{2\pi}B(\gamma)H(\theta',\phi')\sin\theta' d\phi'\ d\theta' \tag{47}$$

where γ is the central angle between (θ,ϕ) and (θ',ϕ'). We have

$$\cos\gamma=\cos\theta\cos\theta'+\sin\theta\sin\theta'\cos(\phi-\phi') \tag{48}$$

The convolution between B and H is thus

$$\begin{aligned}A(\theta,\phi)=&\int_0^{\pi}\int_0^{2\pi}\sum_{l=0}^{\infty}\sqrt{\frac{2l+1}{4\pi}}b_lP_l(\cos\theta\cos\theta'+\sin\theta\sin\theta'\cos(\phi-\phi')) \\ &\times\sum_{k=0}^{\infty}\sum_{m=-k}^{k}H_{km}\sqrt{\frac{(2k+1)}{4\pi}\frac{(k-m)!}{(k+m)!}}P_k^m(\cos\theta')e^{im\phi'}\sin\theta' d\phi'\ d\theta' \qquad (49)\\ =&\sum_{l=0}^{\infty}\sum_{k=0}^{\infty}\sum_{m=-k}^{k}\frac{H_{km}b_l}{4\pi}\sqrt{\frac{(2l+1)(2k+1)(k-m)!}{(k+m)!}} \qquad (50)\\ &\times\int_0^{\pi}\int_0^{2\pi}P_l(\cos\theta\cos\theta'+\sin\theta\sin\theta'\cos(\phi-\phi'))P_k^m(\cos\theta')e^{im\phi'}\sin\theta' d\phi'\ d\theta'\end{aligned}$$

Now [35, 12]

$$\begin{aligned}&\int_0^{2\pi}P_l(\cos\theta\cos\theta'+\sin\theta\sin\theta'\cos(\phi-\phi'))e^{im\phi'}d\phi' \\ =&\int_0^{2\pi}\left[P_l(\cos\theta)P_l(\cos\theta')+2\sum_{j=1}^{l}\frac{(l-j)!}{(l+j)!}P_l^j(\cos\theta)P_l^j(\cos\theta')\cos(j(\phi-\phi'))\right]e^{im\phi'}d\phi' \\ =&\frac{2\pi e^{im\phi}(l-m)!}{(l+m)!}P_l^m(\cos\theta)P_l^m(\cos\theta') \qquad (51)\end{aligned}$$

Substituting this into (50) we now find

$$\begin{aligned}
&\int_0^\pi \frac{2\pi e^{im\phi}(l-m)!}{(l+m)!} P_l^m(\cos\theta) P_l^m(\cos\theta') P_k^m(\cos\theta') \sin\theta' \; d\theta' \\
=&\frac{2\pi e^{im\phi}(l-m)!}{(l+m)!} P_l^m(\cos\theta) \int_0^\pi P_l^m(\cos\theta') P_k^m(\cos\theta') \sin\theta' \; d\theta' \\
=&\frac{2\pi e^{im\phi}(l-m)!}{(l+m)!} P_l^m(\cos\theta) \int_{-1}^1 P_l^m(x) P_k^m(x) dx = \delta_{kl} \frac{4\pi e^{im\phi}}{2l+1} P_l^m(\cos\theta)
\end{aligned} \tag{52}$$

where δ_{kl} is the Kronecker delta. Thus the convolution is

$$\begin{aligned}
A(\theta,\phi) &= \sum_{l=0}^\infty \sum_{k=0}^\infty \sum_{m=-k}^k \frac{H_{km} b_l}{4\pi} \sqrt{\frac{(2l+1)(2k+1)(k-m)!}{(k+m)!}} \times \delta_{kl} \frac{4\pi e^{im\phi}}{2l+1} P_l^m(\cos\theta) \\
&= \sum_{k=0}^\infty \sum_{m=-k}^k H_{km} b_k \sqrt{\frac{(k-m)!}{(k+m)!}} \times P_k^m(\cos\theta) e^{im\phi} \\
&= \sum_{k=0}^\infty \sum_{m=-k}^k H_{km} b_k \sqrt{\frac{4\pi}{2k+1}} Y_k^m(\theta,\phi) = \sum_{k=0}^\infty \sum_{m=-k}^k A_{km} Y_k^m(\theta,\phi)
\end{aligned} \tag{53}$$

where

$$A_{km} = H_{km} b_k \sqrt{\frac{4\pi}{2k+1}} \tag{54}$$

As a special case, the convolution between a circularly symmetric function

$$B(\theta) = \sum_{l=0}^\infty \sqrt{\frac{2l+1}{4\pi}} b_l P_l(\cos\theta) \tag{55}$$

and another one

$$C(\theta) = \sum_{l=0}^\infty \sqrt{\frac{2l+1}{4\pi}} c_l P_l(\cos\theta) \tag{56}$$

is

$$D(\theta) = \sum_{l=0}^\infty \sqrt{\frac{2l+1}{4\pi}} d_l P_l(\cos\theta) \tag{57}$$

where

$$d_l = b_l c_l \sqrt{\frac{4\pi}{2l+1}} \tag{58}$$

i.e.

$$D(\theta) = \sum_{l=0}^\infty b_l c_l P_l(\cos\theta) \tag{59}$$

To find the b_l from $B(\theta)$ we have (55) and thus

$$\begin{aligned}\int_0^\pi B(\theta)P_k(\cos\theta)\sin\theta d\theta =& \sum_{l=0}^\infty \sqrt{\frac{2l+1}{4\pi}}b_l \int_0^\pi P_l(\cos\theta)P_k(\cos\theta)\sin\theta d\theta \\ =& \sqrt{\frac{2k+1}{4\pi}}\frac{2b_k}{2k+1} \end{aligned} \tag{60}$$

and thus

$$b_k = \sqrt{\pi(2k+1)}\int_0^\pi B(\theta)P_k(\cos\theta)\sin\theta d\theta \tag{61}$$

For chimeras on a sphere we will always use the Fisher-von Mises function:

$$B(\theta) = \frac{\kappa e^{\kappa\cos\theta}}{4\pi\sinh\kappa} \tag{62}$$

for which

$$b_k = \frac{\kappa\sqrt{\pi(2k+1)}}{4\pi\sinh\kappa}\int_0^\pi e^{\kappa\cos\theta}P_k(\cos\theta)\sin\theta d\theta \tag{63}$$

Now [12]

$$\begin{aligned}&\int_0^\pi e^{\kappa\cos\theta}P_k(\cos\theta)\sin\theta d\theta = \int_{-1}^1 e^{\kappa x}P_k(x)dx \\ &= i^k\sqrt{\frac{2\pi i}{\kappa}}J_{k+1/2}(-i\kappa) = \sqrt{\frac{2\pi}{\kappa}}I_{k+1/2}(\kappa)\end{aligned} \tag{64}$$

where J is a Bessel function of the first kind and I is a modified Bessel function of the first kind. Thus

$$b_k = \frac{\kappa\sqrt{\pi(2k+1)}}{4\pi\sinh\kappa}\sqrt{\frac{2\pi}{\kappa}}I_{k+1/2}(\kappa) = \frac{\sqrt{2\kappa(2k+1)}}{4\sinh\kappa}I_{k+1/2}(\kappa) \tag{65}$$

To obtain the H_{km} from (44) we use

$$\begin{aligned}&\int_0^\pi\int_0^{2\pi} H(\theta,\phi)Y_j^{-n}(\theta,\phi)d\phi\sin\theta d\theta \\ &= \sum_{k=0}^\infty\sum_{m=-k}^k H_{km}\int_0^\pi\int_0^{2\pi} Y_k^m(\theta,\phi)Y_j^{-n}(\theta,\phi)d\phi\sin\theta d\theta \\ &= 2\pi\sum_{k=0}^\infty H_{kn}\sqrt{\frac{(2k+1)}{4\pi}\frac{(k-n)!}{(k+n)!}}\sqrt{\frac{(2j+1)}{4\pi}\frac{(j+n)!}{(j-n)!}}\int_0^\pi P_k^n(\cos\theta)P_j^{-n}(\cos\theta)\sin\theta d\theta \\ &= 2\pi\sum_{k=0}^\infty H_{kn}\sqrt{\frac{(2k+1)}{4\pi}\frac{(k-n)!}{(k+n)!}}\sqrt{\frac{(2j+1)}{4\pi}\frac{(j+n)!}{(j-n)!}}\frac{(-1)^n(j-n)!}{(j+n)!}\int_0^\pi P_k^n(\cos\theta)P_j^n(\cos\theta)\sin\theta d\theta \\ &= 2\pi\sum_{k=0}^\infty H_{kn}\sqrt{\frac{(2k+1)}{4\pi}\frac{(k-n)!}{(k+n)!}}\sqrt{\frac{(2j+1)}{4\pi}\frac{(j+n)!}{(j-n)!}}\times\frac{2(-1)^n\delta_{kj}}{(2j+1)} = (-1)^n H_{jn}\end{aligned} \tag{66}$$

and thus

$$H_{km} = (-1)^m\int_0^\pi\int_0^{2\pi} H(\theta,\phi)Y_k^{-m}(\theta,\phi)d\phi\sin\theta d\theta \tag{67}$$

Appendix B. Matlab code to generate points on sphere

This code generates cartesian and spherical polar coordinates of points on the unit sphere and allows one to visualise them; code modified from that in [8].

```
N=40;
[xc,yc]=meshgrid(linspace(-3,1,2*N-1),linspace(-1,1,N));
[xp,yp,zp]=thrd(xc,yc);
th=acos(zp);
phi=atan2(yp,xp);
mesh(xp,yp,zp)
```

where

```
function [xp,yp,zp]=thrd(xc,yc)
ijlower=find(xc<-1);
xc(ijlower)=-2-xc(ijlower);
[xp,yp]=mapc2p(xc,yc);
zp=sqrt(1-(xp.^2+yp.^2));
zp(ijlower)=-zp(ijlower);
```

and

```
function [xp,yp] = mapc2p(xc,yc)
r1 = 1;

d = max(abs(xc),abs(yc));  % value on diagonal of computational grid
d = max(d, 1e-10);         % to avoid divide by zero at origin

D=r1*d.*(2-d)/sqrt(2);
R = r1*ones(size(d));

center = D - sqrt(R.^2 - D.^2);
xp = D./d .* abs(xc);
yp = D./d .* abs(yc);

ij = find(abs(yc)>=abs(xc));
yp(ij) = center(ij) + sqrt(R(ij).^2 - xp(ij).^2);
ij = find(abs(xc)>=abs(yc));
xp(ij) = center(ij) + sqrt(R(ij).^2 - yp(ij).^2);

xp = sign(xc) .* xp;
yp = sign(yc) .* yp;
```

Appendix C. Essential spectrum of spirals on a sphere

We now discuss the essential spectrum of spiral waves on a sphere (although the same calculation applies to any fixed point on the sphere). We follow the presentations in [64, 42]. A stationary solution,

$z(\mathbf{r})$, of (6) satisfies

$$0 = -(\Delta - i\Omega)z(\mathbf{r}) + e^{-i\alpha}Z(\mathbf{r})/2 - e^{i\alpha}z^2(\mathbf{r})\overline{Z}(\mathbf{r})/2 \tag{68}$$

where

$$Z(\mathbf{r}) = \int_{\mathbb{S}^2} G(\mathbf{r},\mathbf{r}')z(\mathbf{r}')d\mathbf{r}' \tag{69}$$

Solving the quadratic (68) for $z(\mathbf{r})$ we have

$$z(\mathbf{r}) = \frac{\Delta - i\Omega - \sqrt{(\Delta - i\Omega)^2 + |Z(\mathbf{r})|^2}}{-e^{-i\alpha}Z(\mathbf{r})} \tag{70}$$

where we have to take the negative root so that $|z(\mathbf{r})| \leq 1$. Linearising (6) about this solution we obtain

$$\frac{\partial v(\mathbf{r},t)}{\partial t} = \mu(\mathbf{r})v(\mathbf{r},t) + e^{-i\alpha}V(\mathbf{r},t)/2 - e^{i\alpha}z^2(\mathbf{r})\overline{V}(\mathbf{r},t)/2 \tag{71}$$

where

$$\mu(\mathbf{r}) \equiv -\left(\Delta - i\Omega + e^{i\alpha}z(\mathbf{r})\overline{Z}(\mathbf{r})\right) \tag{72}$$

and

$$V(\mathbf{r}) = \int_{\mathbb{S}^2} G(\mathbf{r},\mathbf{r}')v(\mathbf{r}')d\mathbf{r}' \tag{73}$$

Writing

$$u(\mathbf{r},t) = \begin{pmatrix} \mathrm{Re}[v(\mathbf{r},t)] \\ \mathrm{Im}[v(\mathbf{r},t)] \end{pmatrix} \tag{74}$$

we have $\partial u/\partial t = Lu$ where $L \equiv M + K$, the multiplication operator

$$M = \begin{pmatrix} \mathrm{Re}[\mu(\mathbf{r})] & -\mathrm{Im}[\mu(\mathbf{r})] \\ \mathrm{Im}[\mu(\mathbf{r})] & \mathrm{Re}[\mu(\mathbf{r})] \end{pmatrix} \tag{75}$$

and K is an integral operator corresponding to the last two terms in (71). The essential spectrum of M, $\sigma_{ess}(M)$, consists of all $\lambda \in \mathbb{C}$ such that $\det(M(\mathbf{r}) - \lambda I) = 0$ for some $\mathbf{r} \in \mathbb{S}^2$. Thus

$$\sigma_{ess}(M) = \{\mu(\mathbf{r}) : \mathbf{r} \in \mathbb{S}^2\} \cup \{c.c.\} \tag{76}$$

where "$\{c.c.\}$" is the complex conjugate of the previous set. Using (70) and (72) we have

$$\sigma_{ess}(M) = \left\{-\sqrt{(\Delta - i\Omega)^2 + |Z(\mathbf{r})|^2} : \mathbf{r} \in \mathbb{S}^2\right\} \cup \left\{-\sqrt{(\Delta + i\Omega)^2 + |Z(\mathbf{r})|^2} : \mathbf{r} \in \mathbb{S}^2\right\} \tag{77}$$

Figure 24 shows the numerically calculated eigenvalues of the linearisation of (6) about a stable spiral solution, for two different values of Δ. Also shown is the essential spectrum given by (77) where we used values of $|Z(\mathbf{r})|$ ranging from the minimum to the maximum over $\mathbf{r} \in \mathbb{S}^2$ of the values found for this quantity at the steady state of (6), and the corresponding value of Ω. From (77) we see that the rightmost points of the essential spectrum are $-\Delta \pm i\Omega$, corresponding to the centres of the spirals with $|Z| = 0$. Thus increasing Δ will move this essential spectrum further into the left half plane, separated from the point eigenvalues whose crossing of the imaginary axis is associated with local bifurcations and possible loss of stability of the spirals.

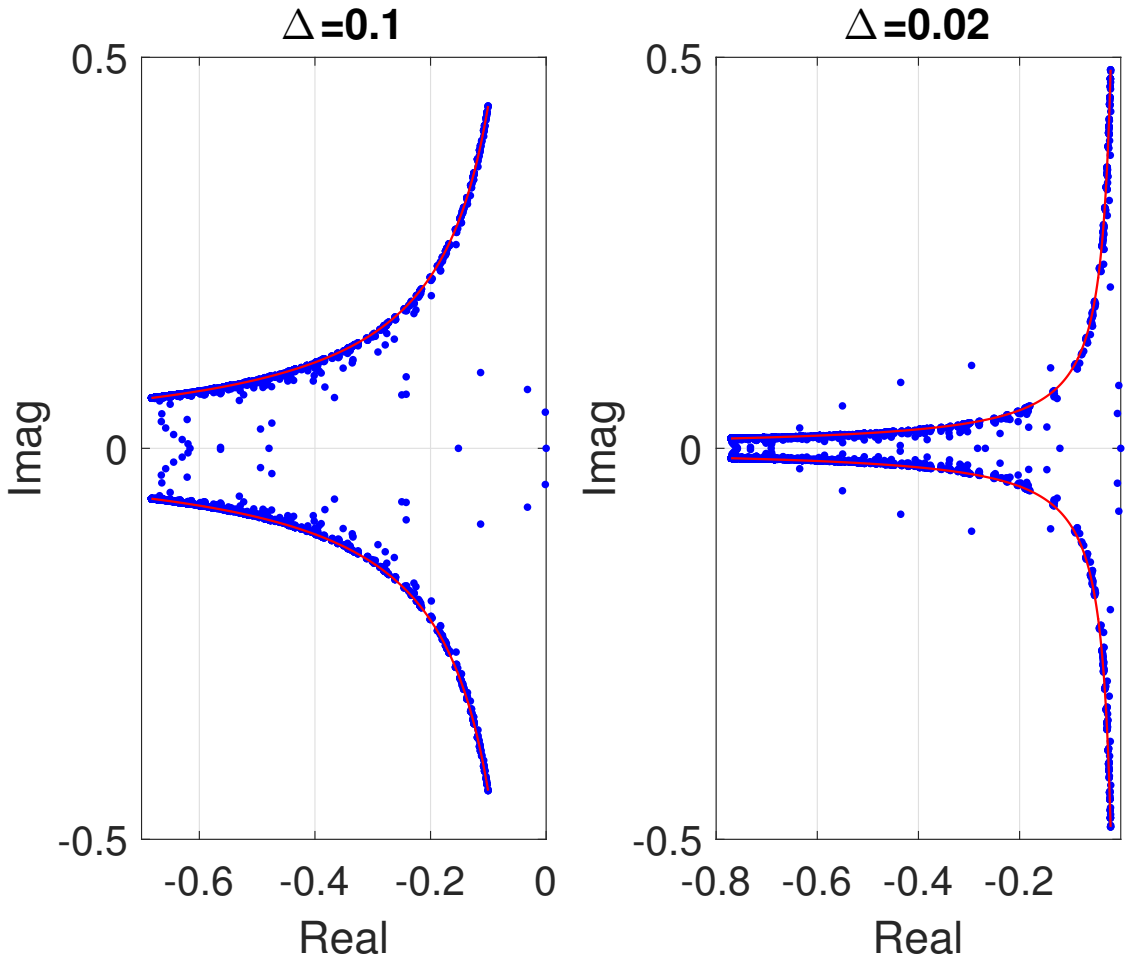

FIGURE 24. Numerically calculated eigenvalues (blue dots) of the linearisation about a stable spiral wave on a sphere for $\Delta = 0.1$ (left); and 0.02 (right). Red curves show the essential spectrum given by (77). Other parameters: $N = 50, M = 20, \alpha = 0.66, \kappa = 10$.

APPENDIX D. SPIRALS WITH D_4-SYMMETRIC COUPLING ARE INDEPENDENT OF λ

This section refers to the model studied in Sec. 3. Spiral waves of interest are steady states of (35), i.e. they satisfy

$$-(\Delta - i\Omega)z(x,y) + e^{-i\alpha}Z(x,y)/2 - e^{i\alpha}z^2(x,y)\overline{Z}(x,y)/2 = 0 \tag{78}$$

where

$$Z(x,y) = \int_{-\pi}^{\pi}\int_{-\pi}^{\pi} G(x-x', y-y'; \lambda) z(x',y') dx'\ dy' \tag{79}$$

and $G(x,y;\lambda)$ is given by (34). We now show that these solutions are independent of λ. Write

$$z(x,y) = R(x,y)\exp\left[i\Theta(x,y)\right] = f(x,y) + ig(x,y) \tag{80}$$

where R, Θ, f and g are real. We see from Fig. 13 that the solution on $[0,\pi]\times[0,\pi]$ is invariant under a rotation in physical space of $\pi/2$ about $(x,y)=(\pi/2,\pi/2)$, as long as $\Theta(x,y)$ is incremented by $\pi/2$. Performing two such rotations we have that $z(\pi-x,\pi-y) = R(x,y)\exp[i\{\Theta(x,y)+\pi\}] = -R(x,y)\exp[i\Theta(x,y)] = -z(x,y)$ and thus $f(\pi-x,\pi-y)=-f(x,y)$ and similarly for g. [We also have $f(-x,y)=f(x,y)$ and $f(x,-y)=f(x,y)$ and similarly for g.] Defining

$$h(x) = \int_{-\pi}^{\pi} f(x,y)\ dy \tag{81}$$

and recalling that y is periodic with period 2π we have

$$h(\pi-x) = \int_{-\pi}^{\pi} f(\pi-x,y)\ dy = \int_{-\pi}^{\pi} f(\pi-x,\pi-y)\ dy = -\int_{-\pi}^{\pi} f(x,y)\ dy = -h(x) \tag{82}$$

Picking just the $\cos(2x)$ term from G, the contribution to Z from f and this term is

$$\begin{aligned}&\int_{-\pi}^{\pi}\int_{-\pi}^{\pi} \cos(2(x-x'))f(x',y')dx'\ dy' \\ &= \cos(2x)\int_{-\pi}^{\pi}\cos(2x')h(x')dx' + \sin(2x)\int_{-\pi}^{\pi}\sin(2x')h(x')dx'\end{aligned} \tag{83}$$

Now (dropping the primes)

$$\int_0^{\pi}\cos(2x)h(x)dx = \int_0^{\pi/2}\cos(2x)h(x)dx + \int_{\pi/2}^{\pi}\cos(2x)h(x)dx \tag{84}$$

Substituting $z=\pi-x$ in the second integral and using (82) we find that

$$\int_0^{\pi}\cos(2x)h(x)dx = \int_0^{\pi/2}\cos(2x)h(x)dx - \int_0^{\pi/2}\cos(2z)h(z)dz = 0 \tag{85}$$

A similar argument shows that $\int_{-\pi}^{0}\cos(2x)h(x)dx=0$, and the even-ness of $h(x)$ gives $\int_{-\pi}^{\pi}\sin(2x)h(x)dx = 0$ and thus the double integral in (83) is equal to zero. These arguments can be repeated replacing f by g and y by x to show that steady states of (35) are independent of λ.

References

[1] D.M. Abrams, R. Mirollo, S.H. Strogatz, and D.A. Wiley. Solvable model for chimera states of coupled oscillators. *Phys. Rev. Lett.*, 101(8):084103, 2008.

[2] D.M. Abrams and S.H. Strogatz. Chimera states for coupled oscillators. *Phys. Rev. Lett.*, 93(17):174102, 2004.

[3] D.M. Abrams and S.H. Strogatz. Chimera states in a ring of nonlocally coupled oscillators. *Int. J. Bifurcat. Chaos*, 16(1):21–37, 2006.

[4] Peter Ashwin and Oleksandr Burylko. Weak chimeras in minimal networks of coupled phase oscillators. *Chaos: An Interdisciplinary Journal of Nonlinear Science*, 25(1):013106, 2015.

[5] Philip J Aston and Carlo R Laing. Symmetry and chaos in the complex Ginzburg-Landau equation-I. Reflectional symmetries. *Dynamics and Stability of Systems*, 14(3):233–253, 1999.

[6] Gilad Barlev, Thomas M. Antonsen, and Edward Ott. The dynamics of network coupled phase oscillators: An ensemble approach. *Chaos*, 21(2):025103, 2011.

[7] Grigory Bordyugov, Arkady Pikovsky, and Michael Rosenblum. Self-emerging and turbulent chimeras in oscillator chains. *Physical Review E*, 82(3):035205, 2010.

[8] D. A. Calhoun, C. Helzel, and R. J. LeVeque. Logically rectangular finite volume grids and methods for circular and spherical domains. *SIAM Review*, 50:723–752, 2008.

[9] Stephen Coombes and Áine Byrne. Next generation neural mass models. In A. Torcini and F. Corinth, editors, *Lecture Notes in Nonlinear Dynamics in Computational Neuroscience: from Physics and Biology to ICT*. Springer, 2016.

[10] Eusebius Doedel, Herbert B Keller, and Jean Pierre Kernevez. Numerical analysis and control of bifurcation problems (i): Bifurcation in finite dimensions. *International journal of bifurcation and chaos*, 1(03):493–520, 1991.

[11] Martin Golubitsky and David G Schaeffer. *Singularities and groups in bifurcation theory*, volume 51 of *Applied Mathematical Sciences*. Springer, 1985.

[12] Izrael Solomonovich Gradshtejn and Iosif Moiseevich Ryzhik. *Table of integrals, series and products*. Academic Press, 1965.

[13] Chad Gu, Ghislain St-Yves, and Jörn Davidsen. Spiral wave chimeras in complex oscillatory and chaotic systems. *Physical review letters*, 111(13):134101, 2013.

[14] A.M. Hagerstrom, T.E. Murphy, R. Roy, P. Hövel, I. Omelchenko, and E. Schöll. Experimental observation of chimeras in coupled-map lattices. *Nature Physics*, 2012.

[15] Y. Kawamura. Chimera Ising walls in forced nonlocally coupled oscillators. *Phys. Rev. E*, 75(5):056204, 2007.

[16] Pan-Jun Kim, Tae-Wook Ko, Hawoong Jeong, and Hie-Tae Moon. Pattern formation in a two-dimensional array of oscillators with phase-shifted coupling. *Phys. Rev. E*, 70(6):065201, Dec 2004.

[17] Y. Kuramoto. *Chemical Oscillations, Waves, and Turbulence*. Springer, Berlin, 1984.

[18] Y. Kuramoto and D. Battogtokh. Coexistence of Coherence and Incoherence in Nonlocally Coupled Phase Oscillators. *Nonlinear Phenom. Complex Syst*, 5(4):380–385, 2002.

[19] Y. Kuramoto and S. Shima. Rotating spirals without phase singularity in reaction-diffusion systems. *Progr. Theor. Phys. Suppl.*, 150:115, 2003.

[20] Carlo R. Laing. Chimera states in heterogeneous networks. *Chaos*, 19(1):013113, 2009.

[21] Carlo R. Laing. The dynamics of chimera states in heterogeneous Kuramoto networks. *Physica D*, 238(16):1569–1588, 2009.

[22] Carlo R. Laing. Chimeras in networks of planar oscillators. *Phys. Rev. E*, 81:066221, Jun 2010.

[23] Carlo R. Laing. Fronts and bumps in spatially extended kuramoto networks. *Physica D*, 240(24):1960 – 1971, 2011.

[24] Carlo R Laing. Disorder-induced dynamics in a pair of coupled heterogeneous phase oscillator networks. *Chaos*, 22(4):043104, 2012.

[25] Carlo R Laing. Derivation of a neural field model from a network of theta neurons. *Physical Review E*, 90(1):010901, 2014.

[26] Carlo R Laing. Numerical bifurcation theory for high-dimensional neural models. *The Journal of Mathematical Neuroscience*, 4(1):13, 2014.

[27] Carlo R Laing. Chimeras in networks with purely local coupling. *Physical Review E*, 92(5):050904, 2015.

[28] Carlo R Laing. Exact neural fields incorporating gap junctions. *SIAM Journal on Applied Dynamical Systems*, 14(4):1899–1929, 2015.

[29] Carlo R Laing, Karthikeyan Rajendran, and Ioannis G Kevrekidis. Chimeras in random non-complete networks of phase oscillators. *Chaos*, 22(1):013132, 2012.

[30] Hon Wai Lau and Jörn Davidsen. Linked and knotted chimera filaments in oscillatory systems. *Phys. Rev. E*, 94:010204, Jul 2016.

[31] Wai Shing Lee, Juan G. Restrepo, Edward Ott, and Thomas M. Antonsen. Dynamics and pattern formation in large systems of spatially-coupled oscillators with finite response times. *Chaos*, 21(2):023122, 2011.

[32] Bing-Wei Li and Hans Dierckx. Spiral wave chimeras in locally coupled oscillator systems. *Physical Review E*, 93(2):020202, 2016.

[33] Tanushree B Luke, Ernest Barreto, and Paul So. Complete classification of the macroscopic behavior of a heterogeneous network of theta neurons. *Neural computation*, 25(12):3207–3234, 2013.

[34] Yuri Maistrenko, Oleksandr Sudakov, Oleksiy Osiv, and Volodymyr Maistrenko. Chimera states in three dimensions. *New Journal of Physics*, 17(7):073037, 2015.

[35] Kamil Maleček and Zbyněk Nádeník. On the inductive proof of legendre addition theorem. *Studia Geophysica et Geodaetica*, 45(1):1–11, 2001.

[36] Erik A. Martens. Bistable chimera attractors on a triangular network of oscillator populations. *Phys. Rev. E*, 82:016216, Jul 2010.

[37] Erik A. Martens, Carlo R. Laing, and Steven H. Strogatz. Solvable model of spiral wave chimeras. *Phys. Rev. Lett.*, 104(4):044101, Jan 2010.

[38] Erik Andreas Martens, Shashi Thutupalli, Antoine Fourrire, and Oskar Hallatschek. Chimera states in mechanical oscillator networks. *Proceedings of the National Academy of Sciences*, 110(26):10563–10567, 2013.

[39] Simbarashe Nkomo, Mark R. Tinsley, and Kenneth Showalter. Chimera states in populations of nonlocally coupled chemical oscillators. *Phys. Rev. Lett.*, 110:244102, Jun 2013.

[40] O.E. Omel'chenko, Y.L. Maistrenko, and P.A. Tass. Chimera States: The Natural Link Between Coherence and Incoherence. *Phys. Rev. Lett.*, 100(4):044105, 2008.

[41] Oleh Omel'chenko, Matthias Wolfrum, and Carlo R Laing. Partially coherent twisted states in arrays of coupled phase oscillators. *Chaos*, 24:023102, 2014.

[42] Oleh E Omel'chenko. Coherence–incoherence patterns in a ring of non-locally coupled phase oscillators. *Nonlinearity*, 26(9):2469, 2013.

[43] Oleh E Omel'chenko, Matthias Wolfrum, and Yuri L Maistrenko. Chimera states as chaotic spatiotemporal patterns. *Physical Review E*, 81(6):065201, 2010.

[44] Oleh E Omel'chenko, Matthias Wolfrum, Serhiy Yanchuk, Yuri L Maistrenko, and Oleksandr Sudakov. Stationary patterns of coherence and incoherence in two-dimensional arrays of non-locally-coupled phase oscillators. *Physical Review E*, 85(3):036210, 2012.

[45] Edward Ott and Thomas M. Antonsen. Low dimensional behavior of large systems of globally coupled oscillators. *Chaos*, 18(3):037113, 2008.

[46] Edward Ott and Thomas M. Antonsen. Long time evolution of phase oscillator systems. *Chaos*, 19(2):023117, 2009.

[47] Mark J. Panaggio and Daniel M. Abrams. Chimera states on a flat torus. *Phys. Rev. Lett.*, 110:094102, Feb 2013.

[48] Mark J Panaggio and Daniel M Abrams. Chimera states: coexistence of coherence and incoherence in networks of coupled oscillators. *Nonlinearity*, 28(3):R67, 2015.

[49] Mark J Panaggio and Daniel M Abrams. Chimera states on the surface of a sphere. *Physical Review E*, 91(2):022909, 2015.

[50] Mark J Panaggio, Daniel M Abrams, Peter Ashwin, and Carlo R Laing. Chimera states in networks of phase oscillators: the case of two small populations. *Physical Review E*, 93(1):012218, 2016.

[51] Diego Pazó and Ernest Montbrió. Low-dimensional dynamics of populations of pulse-coupled oscillators. *Physical Review X*, 4(1):011009, 2014.

[52] A. Pikovsky and M. Rosenblum. Partially integrable dynamics of hierarchical populations of coupled oscillators. *Phys. Rev. Lett.*, 101(26):264103, 2008.

[53] B. Sandstede, A. Scheel, and C. Wulff. Bifurcations and dynamics of spiral waves. *Journal of Nonlinear Science*, 9(4):439–478, 1999.

[54] Arnd Scheel. Bifurcation to spiral waves in reaction-diffusion systems. *SIAM journal on mathematical analysis*, 29(6):1399–1418, 1998.

[55] Gautam C. Sethia, Abhijit Sen, and George L. Johnston. Amplitude-mediated chimera states. *Phys. Rev. E*, 88:042917, Oct 2013.

[56] G.C. Sethia, A. Sen, and F.M. Atay. Clustered chimera states in delay-coupled oscillator systems. *Phys. Rev. Lett.*, 100(14):144102, 2008.

[57] S. Shima and Y. Kuramoto. Rotating spiral waves with phase-randomized core in nonlocally coupled oscillators. *Phys. Rev. E*, 69(3):036213, 2004.

[58] S.H. Strogatz. From Kuramoto to Crawford: exploring the onset of synchronization in populations of coupled oscillators. *Physica D*, 143(1-4):1–20, 2000.

[59] M.R. Tinsley, S. Nkomo, and K. Showalter. Chimera and phase-cluster states in populations of coupled chemical oscillators. *Nature Physics*, 2012.

[60] Lawrence C. Udeigwe and G. Bard Ermentrout. Waves and patterns on regular graphs. *SIAM Journal on Applied Dynamical Systems*, 14(2):1102–1129, 2015.

[61] Sid Visser, Rachel Nicks, and Stephen Coombes. Standing and travelling waves in a spherical brain model: the nunez model revisited. *Physica D*, 2016. submitted.

[62] S. Watanabe and S.H. Strogatz. Integrability of a globally coupled oscillator array. *Phys. Rev. Lett.*, 70:2391–2394, 1993.

[63] S. Watanabe and SH Strogatz. Constants of motion for superconducting Josephson arrays. *Physica D*, 74:197–253, 1994.

[64] M. Wolfrum, O. E. Omel'chenko, S. Yanchuk, and Y. L. Maistrenko. Spectral properties of chimera states. *Chaos*, 21(1):013112, 2011.

[65] Matthias Wolfrum and Oleh E Omel'chenko. Chimera states are chaotic transients. *Physical Review E*, 84(1):015201, 2011.

[66] Jianbo Xie, Edgar Knobloch, and Hsien-Ching Kao. Twisted chimera states and multicore spiral chimera states on a two-dimensional torus. *Physical Review E*, 92(4):042921, 2015.

E-mail address: c.r.laing@massey.ac.nz

Institute of Natural and Mathematical Sciences, Massey University, Private Bag 102-904 NSMC, Auckland, New Zealand., phone: +64-9-414 0800 extn. 43512 fax: +64-9-4418136